

## Distant effect of assimilation of moored currents into a model of coastal wind-driven circulation off Oregon

Alexander L. Kurapov, J. S. Allen, G. D. Egbert, R. N. Miller, P. M. Kosro, M. Levine, and T. Boyd

College of Oceanic and Atmospheric Sciences, Oregon State University, Corvallis, Oregon, USA

Received 5 November 2003; revised 14 May 2004; accepted 17 September 2004; published 22 February 2005.

[1] An optimal interpolation (OI) sequential algorithm is implemented for a three-dimensional primitive equation model to assimilate current measurements from acoustic Doppler profilers moored on the Oregon shelf as a part of the Coastal Ocean Advances in Shelf Transport (COAST) upwelling experiment (May–August 2001). A stationary estimate of the forecast error covariance required by the OI is computed based on the error covariance in the model solution not constrained by data assimilation. Lagged model error covariances are used to account for the effect of previously assimilated data. The forecast error covariance has a shorter alongshore spatial scale than the model error covariance unconstrained by the data, as an effect of propagating dynamical modes. Assimilation of currents from one or two of the moorings located on the path of the upwelling jet helps to improve the model data rms error and correlation at the mooring sites located at an alongshore distance of 90 km, south or north from the assimilation sites. The coastal jet is deflected offshore over Heceta Bank, and assimilation of data from an inner-shelf mooring in the jet separation zone does not help to improve prediction in the far field. Larger improvements are obtained for the first part of the study period (yeardays 146–190). In the second part (days 191–237) the geometry of our limited area model possibly limits prediction accuracy. In numerical experiments involving assimilation of data from only one mooring the actual and expected rms error improvements are compared, providing a consistency test for the forecast error covariance.

**Citation:** Kurapov, A. L., J. S. Allen, G. D. Egbert, R. N. Miller, P. M. Kosro, M. Levine, and T. Boyd (2005), Distant effect of assimilation of moored currents into a model of coastal wind-driven circulation off Oregon, *J. Geophys. Res.*, *110*, C02022, doi:10.1029/2003JC002195.

### 1. Introduction

[2] Modeling and data assimilation (DA) are to become essential components of emerging coastal observatories, providing three-dimensional (3-D) and time-dependent descriptions of the ocean dynamics on the shelf. In the scope of today's extensive observational programs, data assimilative models can serve as tools for data synthesis, or as dynamically based interpolators between observations that remain sparse in space and time.

[3] For applications to the Oregon coast, a high-resolution limited-area circulation model must represent stratified flows over shelf topography and include parameterizations of surface and bottom turbulent boundary layer processes [Allen *et al.*, 1995; Federiuk and Allen, 1995; Oke *et al.*, 2002a, 2002b, 2002c]. Major error sources in such a model are the wind stress, open boundary conditions, model bathymetry and approximations of subgrid turbulent processes. Data assimilation methods use observations inside the modeled area to reduce model solution error and provide an improved description of the ocean state [Bennett, 2002].

These methods can also be used to assess solution error statistics.

[4] In the context of coastal observatories, surface currents from high-frequency (HF) radars [Kosro *et al.*, 1997] and vertical profiles of horizontal currents from moored acoustic Doppler profilers are particularly convenient data sources for assimilation. These instruments sense the currents remotely, providing time series data at fixed points that are most readily combined with models providing an Eulerian description of oceanic flows. Assimilation of HF radar surface currents into models of wind-forced coastal circulation has been a focus of a number of studies [Lewis *et al.*, 1998; Breivik and Sætra, 2001; Oke *et al.*, 2002a], all using a fully nonlinear primitive equation model, realistic data, and a variant of the optimal interpolation (OI) method, in which the model forecast is corrected sequentially based on forecast data differences and a stationary estimate of the forecast error covariance  $\mathbf{P}^f$ .

[5] The present study is to our knowledge the first example of assimilation of depth-dependent velocity measurements from multiple moorings into a 3-D stratified coastal circulation model. Velocity measurements from seven moorings on the mid-Oregon shelf are available for May–August 2001 (Figure 1): six moorings, combined into

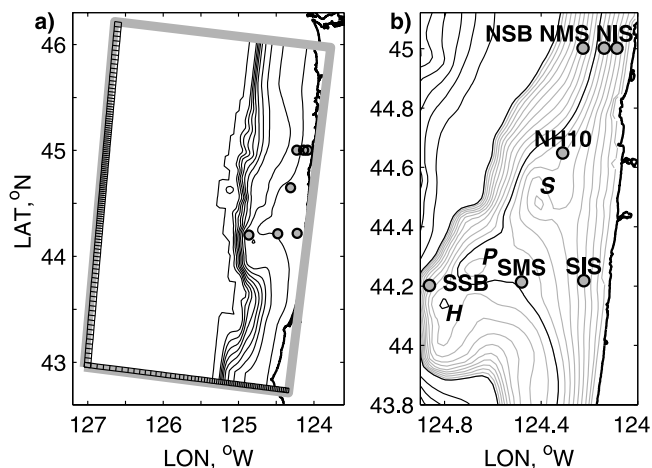


**Figure 1.** Maps of Oregon shelf with circles showing mooring locations in May–August 2001. (a) Computational domain with grid cells along the western and southern boundaries showing the rectangular grid resolution; the bathymetric contour interval is 100 m. (b) Close-up view of the mid-Oregon shelf; the bathymetric contour intervals are 10 m (from 10 to 200 m) for the shaded lines and 100 m for the solid lines. *S*, *P*, and *H* denote banks: Stonewall, Perpetua, and Heceta.

two cross-shore lines 90 km apart, are from the Coastal Ocean Advances in Shelf Transport project (COAST, <http://damp.oce.orst.edu/coast> [Boyd *et al.*, 2002]) while the mooring NH10 is a part of the long-term program on Global Ocean Ecosystem Dynamics (GLOBEC, <http://www.usglobec.org/gaag/overview.html>). We assimilate data from a subset of moorings and validate the solutions against velocity measurements from the moorings not used for assimilation. In this way, the effects of assimilation of distant data on the coastal velocity fields are studied. The effect of velocity assimilation on other oceanographic variables of interest are addressed in a separate manuscript [Kurapov *et al.*, 2005].

[6] The OI method is a zero order approximation of the Kalman filter (KF) [Miller and Cane, 1989]. The KF updates  $\mathbf{P}^f$  each time data are assimilated, which for most oceanographic applications is a prohibitively expensive computational task given the size of  $\mathbf{P}^f$ . Various approximations to the KF, more rigorous than OI, e.g., the reduced rank KF and the ensemble KF have been developed to help overcome the computational demands of the full KF; see Fukumori [2002] for a review on these methods. Owing to their simplicity, OI-type schemes remain a practical tool in operational DA [e.g., Breivik and Sætra, 2001] and in scientific studies, e.g., if the goal is the initial assessment of the value of different data sources in DA [Chen and Wang, 1999; Oke *et al.*, 2002a; Molcard *et al.*, 2003].

[7] In section 2 of this paper, the model setup is described. Model-data comparisons are described in section 3. The details of the OI method are presented in section 4. The distant effect of assimilating currents from a cross-shore line of moorings is discussed in section 5. In section 6 assimilation of currents from a single mooring is considered and the actual performance of DA is compared

to the expectations based on statistical considerations, to provide a consistency test for the forecast error covariance. The role of propagating dynamical modes in OI is discussed in section 7 and a summary is provided in section 8.

## 2. Model Configuration and Mooring Locations

[8] To describe ocean dynamics on the Oregon shelf, we use the Princeton Ocean Model (POM [Blumberg and Mellor, 1987]). The model configuration is similar to that used by Oke *et al.* [2002a, 2002b], where implementation details, omitted here, can be found. The model domain extends 220 km offshore and 350 km alongshore (see Figure 1a). The grid is rectangular with the horizontal ( $x$ ,  $y$ ) axes rotated  $7^\circ$  clockwise from north. The  $x$  axis is then directed toward the coast, and the  $y$  axis is directed alongshore, positive to the north. The velocity components in the ( $x$ ,  $y$ ) directions are ( $u$ ,  $v$ ). The maximum grid resolution is 2 km in the vicinity of Newport ( $44.6^\circ\text{N}$ ), with decreased resolution toward the western, northern and southern boundaries. The vertical resolution is 31  $\sigma$  layers, with eight levels concentrated near the surface and four near the bottom in order to resolve boundary layers. Maximum depth is set at 1000 m. The alongshore boundary conditions are periodic, with the bathymetry and coastline smoothed and matched near the south and north ends of the domain. Offshore boundary conditions are no flow for the depth-averaged  $u$ , no gradient for  $v$ , and radiation for all other variables.

[9] Although solutions obtained with this periodic channel geometry have limitations, some of which are discussed in section 3, extensive model data comparisons documented by Oke *et al.* [2002b] have shown that many important aspects of the shelf flow are successfully represented in this domain. The reason for this success is presumably that off Oregon the coastal currents are strongly wind-driven, with much of the mesoscale behavior on the shelf dominated by local flow-topography interaction. We emphasize that the evaluation of model-only solutions by Oke *et al.* [2002b] includes favorable comparisons with measurements of depth-dependent currents and temperatures from moorings, of surface currents from shore-based HF radars, and of hydrographic measurements from repeated MINIBAT conductivity-temperature-depth (CTD) sections as well as from horizontally extensive SEASOAR CTD surveys. The encouragingly good agreement between the model and observations found in that study motivates the use of a similar model setup for the DA experiments reported here.

[10] A detailed map of the model bathymetry in the area of the COAST observational program is shown in Figure 1b. Near latitude  $45^\circ\text{N}$ , the shelf is narrow with relatively small alongshore variations. Farther to the south the shelf becomes wider and encompasses the topographic irregularities associated with Stonewall Bank, Bank Perpetua, and Heceta Bank. South of Heceta Bank, the shelf narrows again.

[11] The mooring locations are shown in Figure 1. The northern line of moorings, referred to as Line N, is at  $45^\circ\text{N}$ , and includes NSB (North Shelf Break), NMS (North Mid-shelf), and NIS (North Inner Shelf). Correspondingly named

**Table 1.** Acoustic Doppler Profiler Parameters: Manufacturers, Acoustic Frequency, Water Depths of Moorings, and Vertical Resolution of Processed Data

Mooring	Manufacturer	Frequency, kHz	Depth, m	Resolution, m		
				From	To	Interval
NSB	Sontek ADP	250	130	114	18	4
NMS	RDI ADCP	300	81	72	12	2
NIS	RDI ADCP	300	50	42	10	2
NH10	Sontek ADP	500	81	66	10	2
SSB	RDI ADCP	300	132	116	16	4
SMS	Sontek ADP	500	99	91	9	2
SIS	RDI ADCP	300	51	42	8	2

moorings SSB, SMS, and SIS form Line S at 44.2°N. These six moorings are a part of the COAST effort. The seventh, GLOBEC mooring (NH10) is installed midshelf off Newport (44.65°N). Upward looking acoustic Doppler profilers yield horizontal velocities in 2 or 4 m vertical bins with a sampling interval of 120 s. Instrumental parameters including manufacturers, acoustic frequencies, depths of installation, and the vertical data resolution are given in Table 1.

[12] The model is forced with alongshore wind stress and surface heat flux. Wind speed, short wave insolation, air temperature, and relative humidity necessary for the calculation of wind stress and heat flux were measured at a meteorological buoy located next to the NMS mooring. In our limited-area model, these inputs are assumed to be spatially uniform. Heat flux is computed following *Beardsley et al.* [1998] using modeled spatially variable sea surface temperature and surface currents. Since our focus is on subinertial wind-forced ocean variability occurring on temporal scales of several days, the wind stress and the measured variables used for heat flux computation are low-pass filtered with a 40 hour half amplitude filter. The mooring data used for assimilation and validation and the model time series used for statistical analysis are low-pass filtered as well.

[13] Initial conditions for model runs are zero velocity and horizontally uniform potential temperature  $T$  and salinity  $S$ , with vertical profiles of  $T$  and  $S$  taken as the mean observed profiles from June, 1961–1971, at a

station 45 nautical miles offshore of Newport. The model is spun-up with southward alongshore wind stress of constant magnitude 0.05 Pa for 10 days, followed by a 5 day relaxation period with no wind. After the end of this 15 day spin-up, beginning on yearday 141 (the first day when data from all the 7 moorings are available), observed wind stress and heat flux are applied. Data assimilation starts on the same day and the model is run for 96 days, covering the period of operation of the COAST moorings.

[14] A relatively short spin-up period is chosen because of limitations the periodic channel puts on the length of the model run. The study of *Oke et al.* [2002b] showed that the solution quality can be sensitive to the choice of initial spatially uniform  $T$  and  $S$  profiles. At the outset, we performed similar sensitivity studies using historical vertical profiles at different distances from coast and averaged over different periods (May, June, spring, or summer). The profiles that provided the best results in terms of model data velocity statistics were then used for data assimilation experiments. Further tests were conducted to verify that the choice of initial  $T$  and  $S$  does not affect our conclusions about the distant effect of data assimilation.

### 3. Data-Model Comparison

[15] During the study period, wind stress is predominantly southward and upwelling favorable (Figure 2). Figure 3a shows the time-averaged model surface currents and local flow Rossby number, i.e., the time-averaged surface vorticity divided by the Coriolis parameter  $f$ :  $\zeta/f = (v_x - u_y)/f$ , where subscripts denote differentiation. The standard deviation of  $\zeta/f$  and the streamlines of the time-averaged depth-integrated transport from the model solution without DA are shown in Figure 3d. The upwelling jet generally follows bathymetry and detaches from the coast south of Line N. The values of  $\zeta/f$  are close to 1 on the inshore side of the jet, indicating the importance of nonlinear advective effects in that part of the flow. The jet crosses isobaths and separates toward deep water south of Heceta Bank (43.9°N), where the shelf narrows again.

[16] Modeled and observed time series of the depth-averaged velocity at the mooring sites are shown in Figure 4.

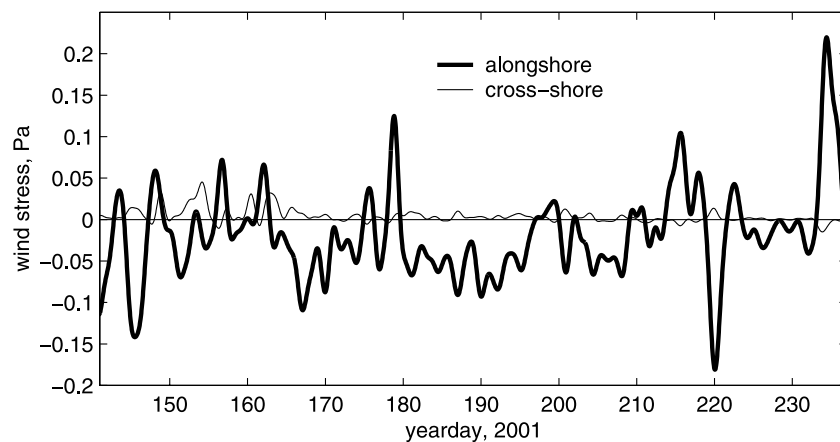


**Figure 2.** Wind stress during the Coastal Ocean Advances in Shelf Transport (COAST) 2001 upwelling experiment. The alongshore component has a time average of  $-0.020$  Pa and a standard deviation of  $0.054$  Pa.

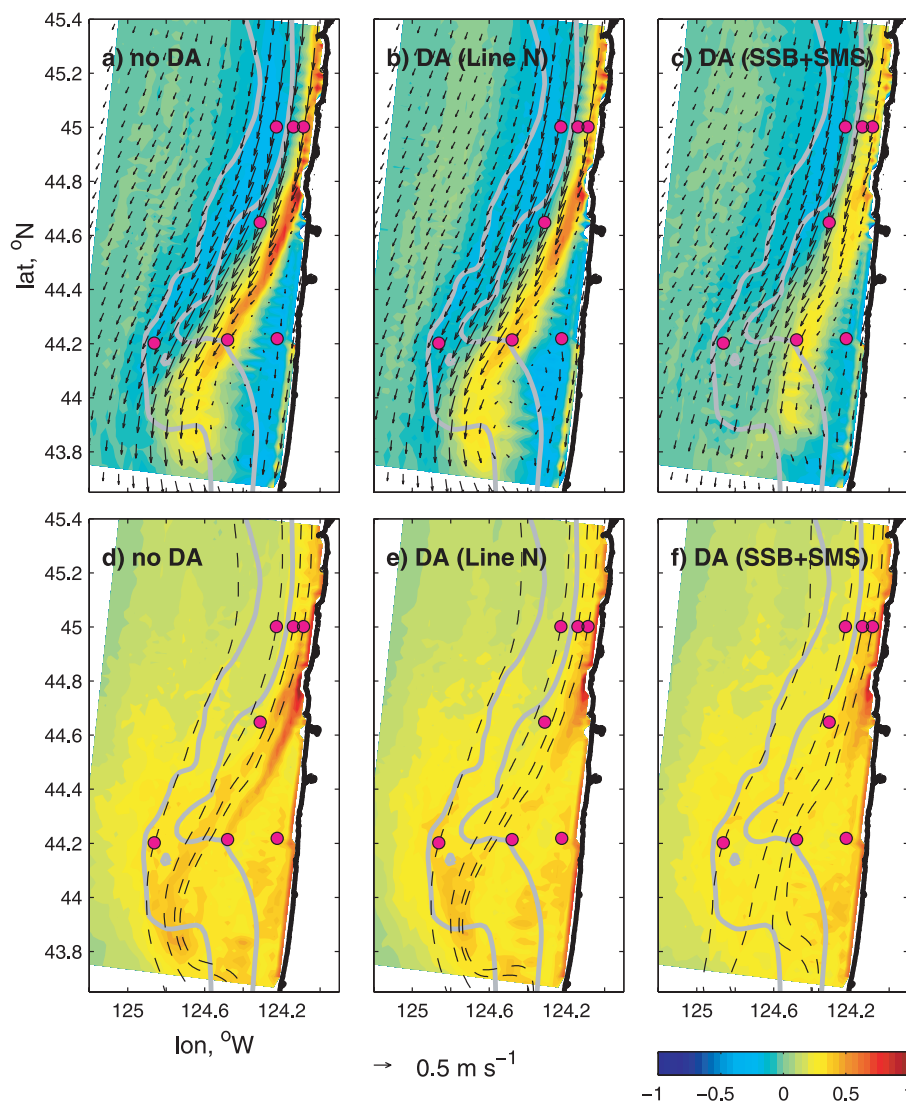


**Figure 3.** Maps of surface current, surface scaled vorticity  $\zeta/f$ , and streamlines of depth-integrated transport, days 146–191. (top) Time-averaged surface current (vectors) and  $\zeta/f$  (color). (bottom) Standard deviation of  $\zeta/f$  (color) and time-averaged transport streamlines (dashed contours) through locations NSB, NMS, NIS, and SSB. (a, d) Model-only solution. (b, e) DA (NSB+NMS). (c, f) DA (SSB+SMS).

Qualitatively, model data agreement is better at the moorings on the more alongshore uniform narrow shelf (Line N) and at the inner-shelf mooring of Line S. At SSB the modeled current is significantly larger than observed, especially after day 191. A possible explanation for the discrepancy at SSB, and the statistics of model data differences at the mooring sites, are discussed below.

[17] In Figure 5, temperature time series from the model and from the six COAST moorings are compared at depths near the surface and close to 20 m. Model temperatures are generally close to observations, indicating that evolution of the model temperature fields from specified initial values (as influenced by upwelling flow processes and by surface heat flux) is in general reasonably accurate. However, at SSB, the model is erroneously warmer (at both depths) during days 190–220. This behavior does not appear to result from overheating the water mass repeatedly reentering the periodic channel, since the temperature at the Line N

is correct for those days. After day 220, model temperature at SSB returns more closely to observed values.

[18] To help understand the reasons for the poor model performance at SSB in the second part of the study period it is instructive to examine available AVHRR satellite SST images. On day 183 (Figure 6a), upwelled water colder than about  $12^{\circ}\text{C}$  is confined to the shelf, with the offshore extent of this observed cold surface water similar at the southern and northern ends of our periodic channel. On day 189 (Figure 6b), upwelled water is still confined to the 200 m isobath in the area near the moorings. At the same time, however, current separation off Cape Blanco, at the southern edge of our domain near  $43^{\circ}\text{N}$ , is apparent. This feature is not represented accurately in our periodic channel setup. In the images on days 205 and 211 (Figures 6c and 6d), patches of upwelled water ( $12^{\circ}$ – $14^{\circ}\text{C}$ ) are seen to extend to the west of the mid-Oregon shelf, where the moorings are installed. These images evidently reflect large offshore

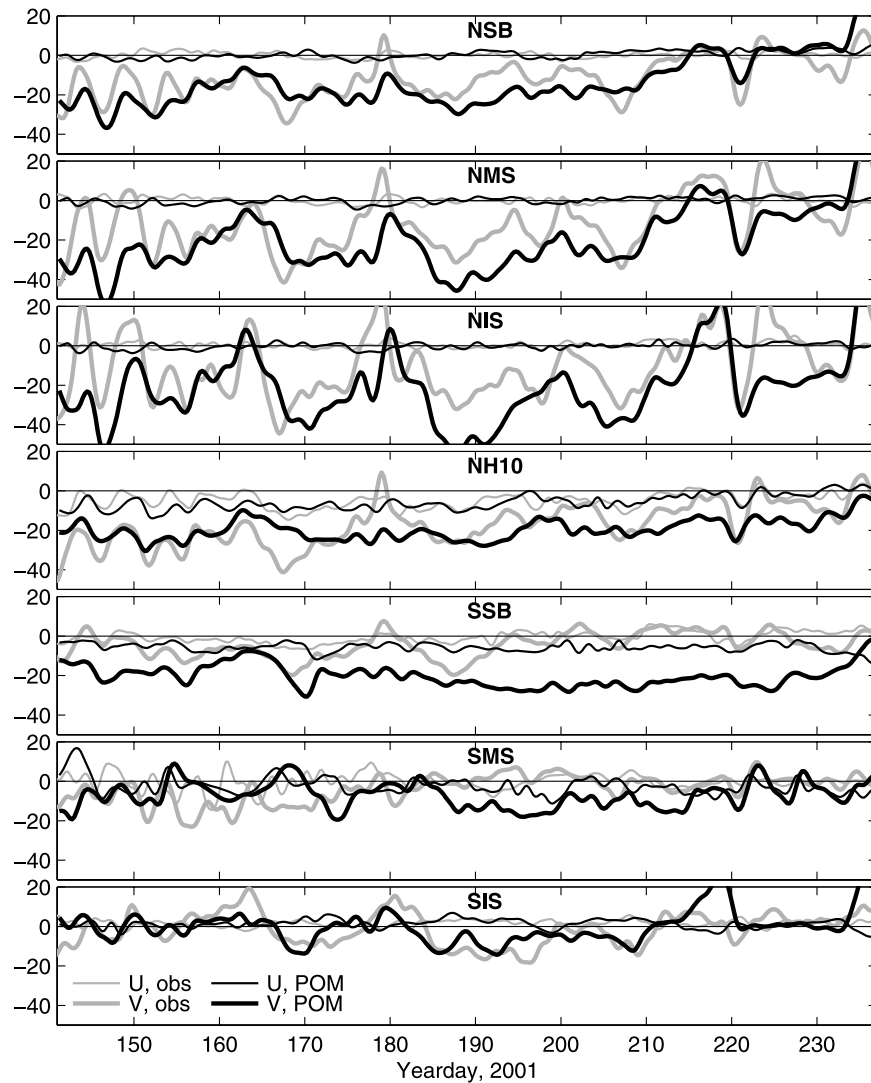


**Figure 4.** Time series of depth-averaged current ( $\text{cm s}^{-1}$ ) at the seven mooring locations: model-only solution (solid line), data (shaded line),  $u$  (thin line), and  $v$  (bold line). Statistical comparisons are recorded in Table 2.

fluctuations of the coastal jet that are not easily reproduced by the periodic channel model. This may explain the discrepancy between modeled and observed currents and temperature at the SSB in the model after day 190. Maps of surface HF radar currents averaged over the first and second halves of the study period (P. M. Kosro, personal communication, 2003) show that the upwelling jet is deflected significantly to the west during the second half, consistent with impressions from the SST maps. Although the reasons for the westward flow separation around Heceta Bank that contributes to the mesoscale activity offshore are still not entirely understood, it is possible that these events off the mid-Oregon shelf are dynamically coupled with the separation off Cape Blanco, 100–150 km to the south, by the northward propagation of shelf flow disturbances as coastal trapped waves. If so, remote forcing would be significant for the ocean dynamics near SSB at least during the second part of the study period and the limited-area periodic channel model used here would not be capable of reproducing these separation effects.

[19] Statistical analyses of modeled and observed velocities are performed using time series for the first part of the study period (days 146–191). The model data rms errors for each mooring site are computed as

$$\text{RMSE} = \left[ \frac{1}{2NK} \sum_{j=1}^N \sum_{k=1}^K \left( u_{k,j} - u_{k,j}^o \right)^2 + \left( v_{k,j} - v_{k,j}^o \right)^2 \right]^{1/2}, \quad (1)$$

where index  $k$  refers to vertical level (velocity bin) and index  $j$  to time. The complex correlation is defined as the correlation of the predicted and observed complex time series  $u + iv$ , where  $i = \sqrt{-1}$  [Kundu, 1976]. For RMSE and correlation analysis, modeled  $(u, v)$  and observed  $(u^o, v^o)$  time series are sampled each  $T_I/4$ , where  $T_I \approx 17$  h is the inertial period. The RMSE values for the model only and for all the DA runs discussed here and the amplitudes of the complex correlation of the depth-averaged modeled and observed currents are given in Table 2. Applied to the wind-driven circulation off Oregon, the 95% confidence limit for

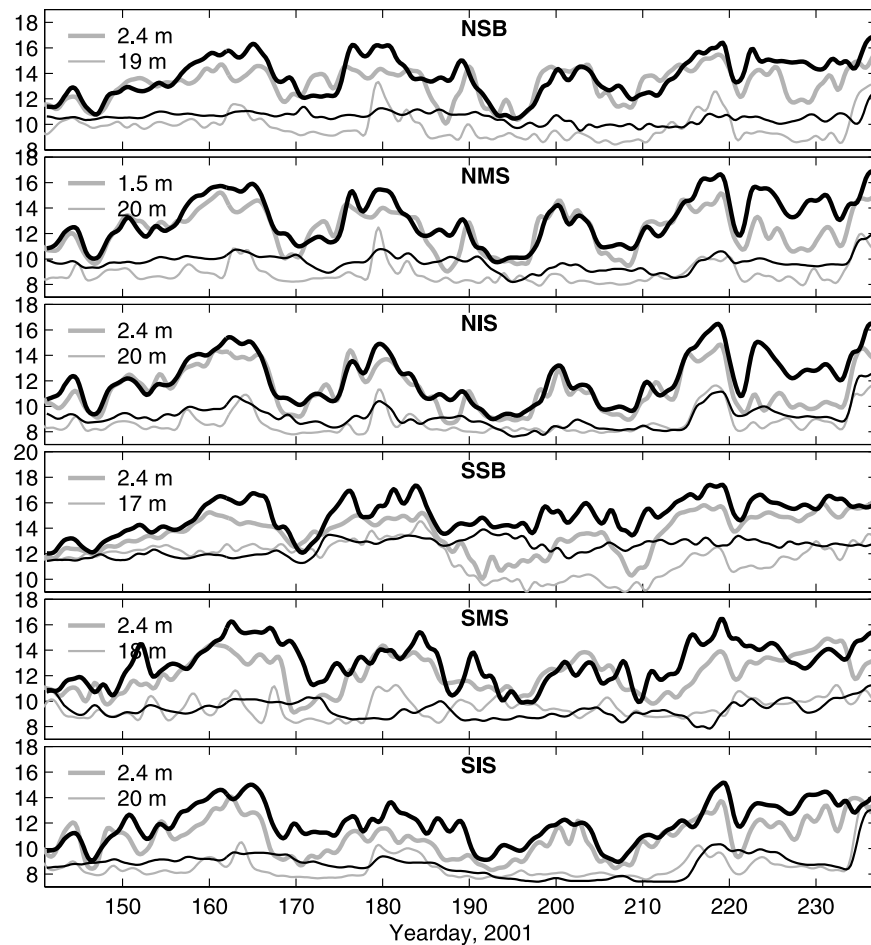


**Figure 5.** Temperature time series at the moorings on lines N and S: model solution (solid line) and data (shaded line). Bold lines are for a sensor closest to the surface, and thin lines for the depth close to 20 m.

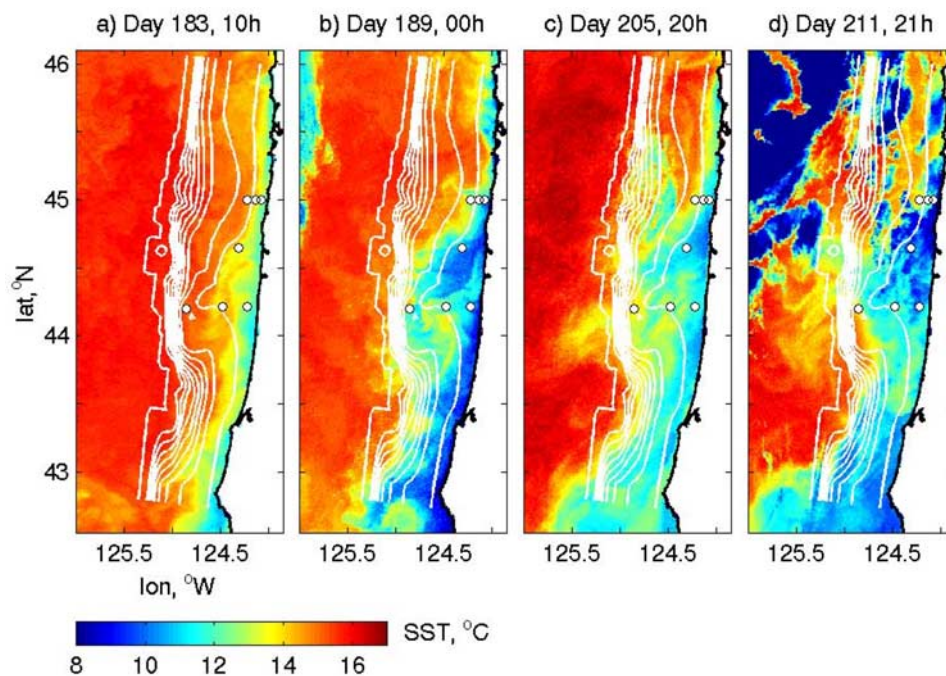


**Figure 6.** Advanced Very High Resolution Radar (AVHRR) sea surface temperature (SST) images. White contours are model bathymetry, each 100 m; circles show mooring locations.

**Table 2.** Model Data Velocity Error Statistics at the Mooring Sites Calculated for Days 146–191: Root-Mean-Square Error (RMSE) and Amplitude of Complex Correlation of the Depth-Averaged Currents<sup>a</sup>

Case	NSB	NMS	NIS	NH10	SSB	SMS	SIS
<i>RMSE, m s<sup>-1</sup></i>							
No DA	6.7	11.3	13.5	7.8	9.6	10.6	5.5
NSB+NMS	3.6	5.6	8.0	5.8	7.1	9.5	6.1
Line N	3.5	5.1	5.9	5.5	6.6	9.1	6.0
SSB+SMS	5.0	7.9	10.8	6.9	3.5	5.6	5.4
Line S	4.7	9.0	12.2	5.6	4.1	5.6	3.5
NSB	4.1	7.2	10.1	6.4	7.3	10.0	6.1
NMS	4.0	5.7	8.5	5.7	7.3	9.7	5.8
NIS	4.7	6.0	6.1	5.8	7.2	10.3	6.3
NH10	4.5	6.9	9.1	4.7	8.0	9.1	6.2
SSB	6.3	10.4	12.9	7.7	3.6	9.3	4.8
SMS	5.8	10.6	12.9	6.8	9.8	6.9	5.3
SIS	8.1	14.1	17.0	12.5	10.9	9.9	4.5
<i>Amplitude of Complex Correlation</i>							
No DA	0.45	0.46	0.56	0.18	0.36	0.26	0.69
NSB+NMS	0.87	0.90	0.82	0.71	0.70	0.09	0.59
Line N	0.88	0.93	0.93	0.74	0.73	0.08	0.59
SSB+SMS	0.82	0.79	0.71	0.63	0.85	0.68	0.69
Line S	0.75	0.69	0.62	0.73	0.78	0.68	0.92
NSB	0.82	0.82	0.73	0.65	0.65	0.08	0.58
NMS	0.84	0.89	0.79	0.72	0.75	0.12	0.64
NIS	0.72	0.87	0.92	0.69	0.73	0.26	0.50
NH10	0.77	0.82	0.79	0.83	0.66	0.09	0.55
SSB	0.69	0.71	0.62	0.67	0.87	0.30	0.79
SMS	0.76	0.68	0.72	0.47	0.45	0.54	0.75
SIS	0.33	0.41	0.46	0.18	0.18	0.14	0.85

<sup>a</sup>Italicized values are for the sites where data are assimilated.

correlations using 45 day time series is estimated to be about 0.5, similar to that found by *Oke et al.* [2002a]. At Line N, model data correlations for the depth-averaged currents for days 146–191 are near this limit; at SIS the correlation is higher (0.69), and at NH10, SSB, and SMS, where the flow is significantly complicated by the three-dimensional bathymetry, correlations are low and not statistically significant.

[20] The model describes variability of currents adequately in terms of some criteria that are less stringent than the

model data rms error and correlation. For instance, variance ellipses of the depth-averaged currents from the model and the observations are close at all six mooring sites of Lines N and S (Figure 7a), although the model significantly underestimates the variance at NH10. Also, the modeled mean depth-averaged currents at all moorings on Line N and at SSB are larger than observed. From the time-averaged alongshore velocity profiles (Figure 8 (top)) we see that the model correctly reproduces vertical mean shear over the depth range of the velocity observations. In Figure 8 (bottom) we compare alongshore components of the 1st empirical orthogonal functions (EOFs) computed separately for each mooring location, and we find similarity between dominant modes of variability for the model and observations. In both cases the 1st EOF for each mooring explains more than 30% of flow variability.

#### 4. Data Assimilation Method

[21] The optimal interpolation (OI) DA algorithm we use provides corrections to the model forecast solution sequentially based on the forecast data differences. The corrected analysis solution provides initial conditions for the next forecast:

$$\mathbf{w}_t^a = \mathbf{w}_t^f + \mathbf{G}(\mathbf{d}_t - \mathbf{H}\mathbf{w}_t^f), \quad (2)$$

where  $\mathbf{w}_t^f$  and  $\mathbf{w}_t^a$  are the forecast and analysis state vectors at time  $t$ , vector  $\mathbf{d}_t$  is the data at this time, matrix  $\mathbf{H}$  is the data functional matching the state vector to the data, and  $\mathbf{G}$  is the gain matrix that is used to extrapolate observation forecast differences onto the whole state space. The definition of  $\mathbf{G}$  is based on the Kalman filter theory [e.g., *Miller and Cane, 1989*]:

$$\mathbf{G} = \mathbf{P}^f \mathbf{H}' (\mathbf{H} \mathbf{P}^f \mathbf{H}' + \mathbf{C}_d)^{-1}, \quad (3)$$

where  $\mathbf{P}^f$  is the forecast error covariance,  $\mathbf{C}_d$  is the data error covariance, and the prime denotes matrix transpose. If estimates of  $\mathbf{P}^f$  and  $\mathbf{C}_d$  are correct and if the errors in the

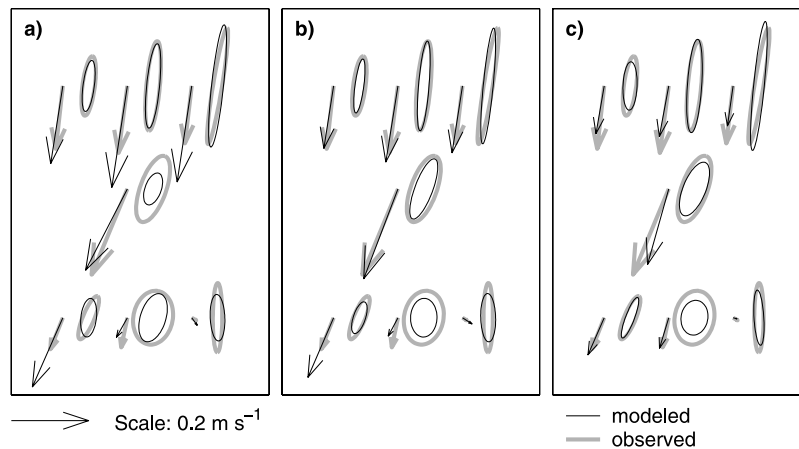


**Figure 7.** Mean and variance ellipses of the depth-averaged current at mooring locations, observations (shaded), and a model solution (solid), days 146–191: (a) no DA, (b) DA (NSB+NMS); and (c) DA (SSB+SMS). In each plot the top row from left to right is NSB, NMS, and NIS, the middle row is NH10; and the bottom row from left to right is SSB, SMS, and SIS.

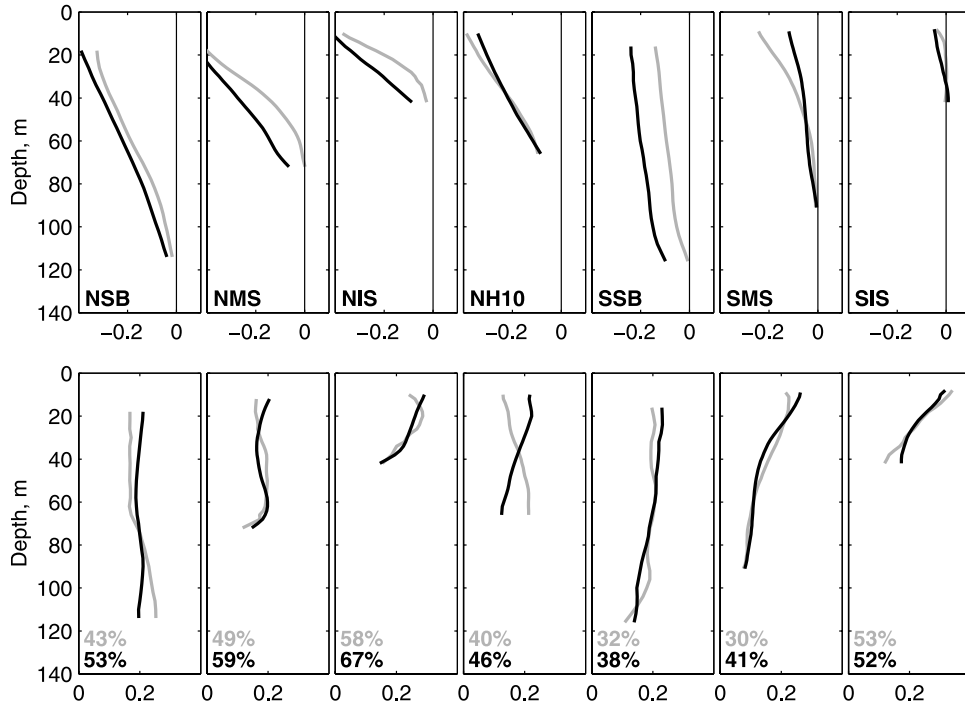


**Figure 8.** Vertical profiles of (top) mean alongshore currents at the mooring sites and (bottom) alongshore component of the 1st empirical orthogonal function (EOF) computed separately for each mooring site, days 146–191, model-only solution (solid lines) and observations (shaded lines). Numbers show the percentage variance explained by the EOF.

forecast and data are statistically unbiased, each element of  $\mathbf{w}_t^a$  has the minimum error variance among all possible solutions. Possible forecast bias in our model is discussed in the end of section 5.

[22] In OI a time-invariant  $\mathbf{P}^f$  is assumed. In principle,  $\mathbf{P}^f$  may indeed become stationary after a long enough integration time, for instance, if the dynamical system is autonomous (model propagator is time invariant) and dissipative, data are assimilated at equal time intervals, and  $\mathbf{H}$  and  $\mathbf{C}_d$  do not change with time [Kurapov *et al.*, 2002]. In the context of a primitive equation coastal model, the assumption that  $\mathbf{P}^f$  is stationary is certainly an approximation that yields a suboptimal analysis. For instance, advection, known to be significant in this system, makes  $\mathbf{P}^f$  state-dependent. So, in OI, optimality is traded for computational efficiency. Note that although  $\mathbf{P}^f$  is of tremendous size, only a much smaller matrix  $\mathbf{P}^f \mathbf{H}'$  is needed in (3). In the case of direct measurements of the elements of the state vector, each column of  $\mathbf{P}^f \mathbf{H}'$  is the forecast error covariance between all elements of the state vector and a measured variable. An estimate of the forecast error covariance, conditioned upon previously assimilated data, can be computed using the estimate of the error covariance in the model-only solution not constrained by the data [Kurapov *et al.*, 2002]:

$$\mathbf{P}^f \mathbf{H}' = \mathbf{P}_{t,t}^m \mathbf{H}' - \mathbf{S}(\mathbf{Q} + \mathbf{C})^{-1} \mathbf{S}' \mathbf{H}'. \quad (4)$$

Here  $\mathbf{P}_{s,q}^m$  is the covariance of errors in the model estimates  $\mathbf{w}$  at times  $s$  and  $q$  (in a solution without DA);  $\mathbf{S} = \{\mathbf{P}_{t,1}^m \mathbf{H}' | \mathbf{P}_{t,2}^m \mathbf{H}' | \dots | \mathbf{P}_{t,t-1}^m \mathbf{H}'\}$  are lagged model error covariances, where the second subscript index in

each block refers symbolically to the past assimilation time;  $\mathbf{Q}$  is the matrix with block elements  $\mathbf{H} \mathbf{P}_{s,q}^m \mathbf{H}'$ ,  $1 \leq q$ ,  $s \leq t - 1$ ; and  $\mathbf{C}$  is block diagonal with  $\mathbf{C}_d$  replicated on the main diagonal. The relation in (4) has been derived under an assumption that data errors are not correlated in time. We retain this assumption for the sake of simplicity, even though data filtering implies a nonzero temporal decorrelation scale for the data errors. Since we find a stationary estimate of the forecast error covariance, no time index is associated with the notation for  $\mathbf{P}^f$ . For  $\mathbf{P}_{s,q}^m$  time indices are retained to refer to time lags. The model error covariance  $\mathbf{P}_{s,q}^m$  required in (4) is assumed to depend only on the time lag  $s - q$ .

[23] To estimate  $\mathbf{P}_{s,q}^m \mathbf{H}'$ , the generalized inverse theory could in principle be employed. In the language of the variational generalized inverse method [e.g., Bennett, 2002], columns of  $\mathbf{P}_{s,q}^m \mathbf{H}'$  are representors evaluated at time  $s$  corresponding to the measurements  $\mathbf{H}$  at time  $q$ . Thus estimates of the model error covariance  $\mathbf{P}_{s,q}^m$  necessary for the computation of  $\mathbf{P}^f$  could be obtained from a series of runs using a tangent linear and adjoint codes. At present, these tools in a form applicable to a coastal circulation problem are in the development stage [Moore *et al.*, 2004]. Here, to obtain an approximate stationary estimate of  $\mathbf{P}_{s,q}^m$  we resort to an ensemble technique. Similar to Oke *et al.* [2002a], a stationary estimate of the model error covariance is assumed to be proportional to the model state covariance:

$$\text{Cov}(w_i, w_j) = \text{Std}(w_i) \text{Std}(w_j) \text{Corr}(w_i, w_j), \quad (5)$$

where  $w_i$  and  $w_j$  are elements of the state vector, and the standard deviation (Std) and the correlation coefficient (Corr) are computed by temporal averaging. In our study, to obtain stable model statistics, model correlation coefficients in (5) are first obtained for each solution from an ensemble of nine 50 day model runs. Each run was forced with observed winds for May–June for different years between 1992 and 2002 and with heat flux based on the time-varying air temperature observed for the same years at a NOAA National Data Buoy Center (NDBC) buoy (44.62°N, 124.53°W), seasonally varying short wave insolation, and constant relative humidity (85%). Since upwelling intensity changes from year to year, to obtain the model error covariance the correlations in (5) are scaled with standard deviations computed for summer 2001. Note, that since time averaging is involved, the number of degrees of freedom in the ensemble of model states used to estimate stationary statistics is equal to the number of model solutions (nine) times the number of degrees of freedom in a 50 day low-pass filtered model time series, which is approximately 15 [see *Oke et al.*, 2002a].

[24] In theory,  $\mathbf{P}_{t,s}^m$  is defined as  $\langle \delta \mathbf{w}_t^m \delta \mathbf{w}_s^m \rangle$ , where  $\delta \mathbf{w}^m = \mathbf{w}_t^m - \mathbf{w}_t$  is the difference between the model solution and the truth at time  $t$ , and  $\langle \rangle$  denote an average over an hypothetical ensemble generated in accordance with the assumed statistics of errors in inputs (forcing, initial, and boundary conditions) [see *Bennett*, 2002]. In our case, where  $\mathbf{P}_{t,s}^m$  is based on (5), ensemble averaging is replaced with temporal averaging under the assumption of stationarity, and the unknown true state is replaced with the time mean. Despite these approximations our estimate of  $\mathbf{P}_{t,s}^m$  should represent correctly the spatiotemporal error correlations associated with alongshore advection and coastal trapped wave propagation. For instance, since the error is advected with the current, we expect similarly higher correlations along the path of the upwelling jet both for modeled velocities and their errors.

[25] In the way the ensemble of model runs used for estimating  $\mathbf{P}^m$  was generated, model solution error is associated implicitly with uncertainty in the wind. In fact, other error sources such as boundary and initial conditions, unresolved small-scale processes, etc. may also be important. On the basis of theoretical analysis of the error covariance evolution in a simplified coastal ocean problem [Kurafov et al., 2002], the spatiotemporal structure of additive components of  $\mathbf{P}^m$  associated with these different error sources is expected to be similar, defined primarily by the direction and speed of advection and coastal trapped wave propagation and to be represented well by the covariance computed as described above.

[26] In this study we choose to provide correction only to velocities  $u$  and  $v$ , and allow other variables (SSH, potential temperature  $T$ , salinity  $S$ , etc.) to evolve as a result of dynamical adjustment. So, in (2)–(4), elements in rows of  $\mathbf{P}^f \mathbf{H}^f$  corresponding to those other variables are zeros. Although forecast errors in the velocity are in general correlated with errors in the scalar fields, such as  $T$  and  $S$ , the cross correlation estimated in the way described above is probably not always adequate. For instance, the approach setting cross correlations between velocities and other fields to zero was found to be more accurate for the prediction of  $T$  than that based on a fully multivariate forecast covariance.

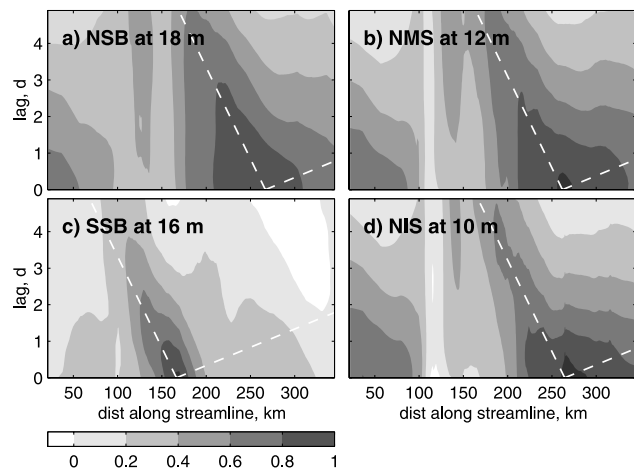


**Figure 9.** Lagged model solution correlation of  $v_\tau(s, t)$  and  $v_\tau(s_o, t - \text{lag})$ , where  $v_\tau$  is the model velocity tangent to the mean depth-integrated transport streamline, taken at a constant depth corresponding to the depth of the measurement location,  $s$  is the distance along the streamline (measured from the south boundary), and  $s = s_o$  is the measurement location. For reference, dashed white lines show characteristics of waves of type (8) traveling with the speed of  $c = -20 \text{ km d}^{-1}$  to the left and  $c = 100 \text{ km d}^{-1}$  to the right, coming through the observation location at zero lag. Measurement sites are (a) NSB at 18 m, (b) NMS at 12 m, (c) SSB at 16 m, and (d) NIS at 10 m.

Note that in the case of a geostrophically balanced alongshore current, velocity contains information only about density gradient, not the density itself. However, in our case the OI with a fully multivariate  $\mathbf{P}^f$  would provide changes to the density based on velocity forecast data misfits.

[27] Lagged model covariances have not been used before for the computation of  $\mathbf{P}^f$  based on (4) in a realistic setting. *Oke et al.* [2002a] essentially assumed that  $\mathbf{P}^f = \alpha \mathbf{P}_{t,t}^m$ , with the coefficient  $\alpha$ ,  $0 < \alpha < 1$ , tuned to provide the best fit to independent data. Although such an assumption may yield a practically satisfactory analysis, the use of (4) is more methodologically correct and not significantly more difficult. The reduction of variance in  $\mathbf{P}^f$ , compared to  $\mathbf{P}_{t,t}^m$ , is modeled explicitly as the effect of previously assimilated data. Also, as shown by *Kurafov et al.* [2002], (4) implies that the spatial structure of  $\mathbf{P}_{t,t}^m$  and  $\mathbf{P}^f$  can be different. We consider this issue further in section 7.

[28] In the computation of lagged model error correlations we restrict ourselves to using lags  $\leq 5$  days. Model correlations for larger lags are small and can be neglected (Figure 9). The panels in Figure 9 show the correlations of the model velocity components  $v_\tau(\mathbf{x}, t)$  with  $v_\tau(\mathbf{x}_o, t - \text{lag})$ , where  $v_\tau$  is the horizontal velocity tangent to the mean transport streamline through the observation location (Figure 3d),  $\mathbf{x}$  denotes the point along this streamline at the observation depth, and  $\mathbf{x}_o$  is the observation location. The correlations are shown as functions of the distance along the streamline and the lag.

[29] In the spatiotemporal structure of  $\mathbf{P}_{t,s}^m$ , defined here by lagged correlations, we should expect to see characteristics corresponding to propagating modes of a (tangent

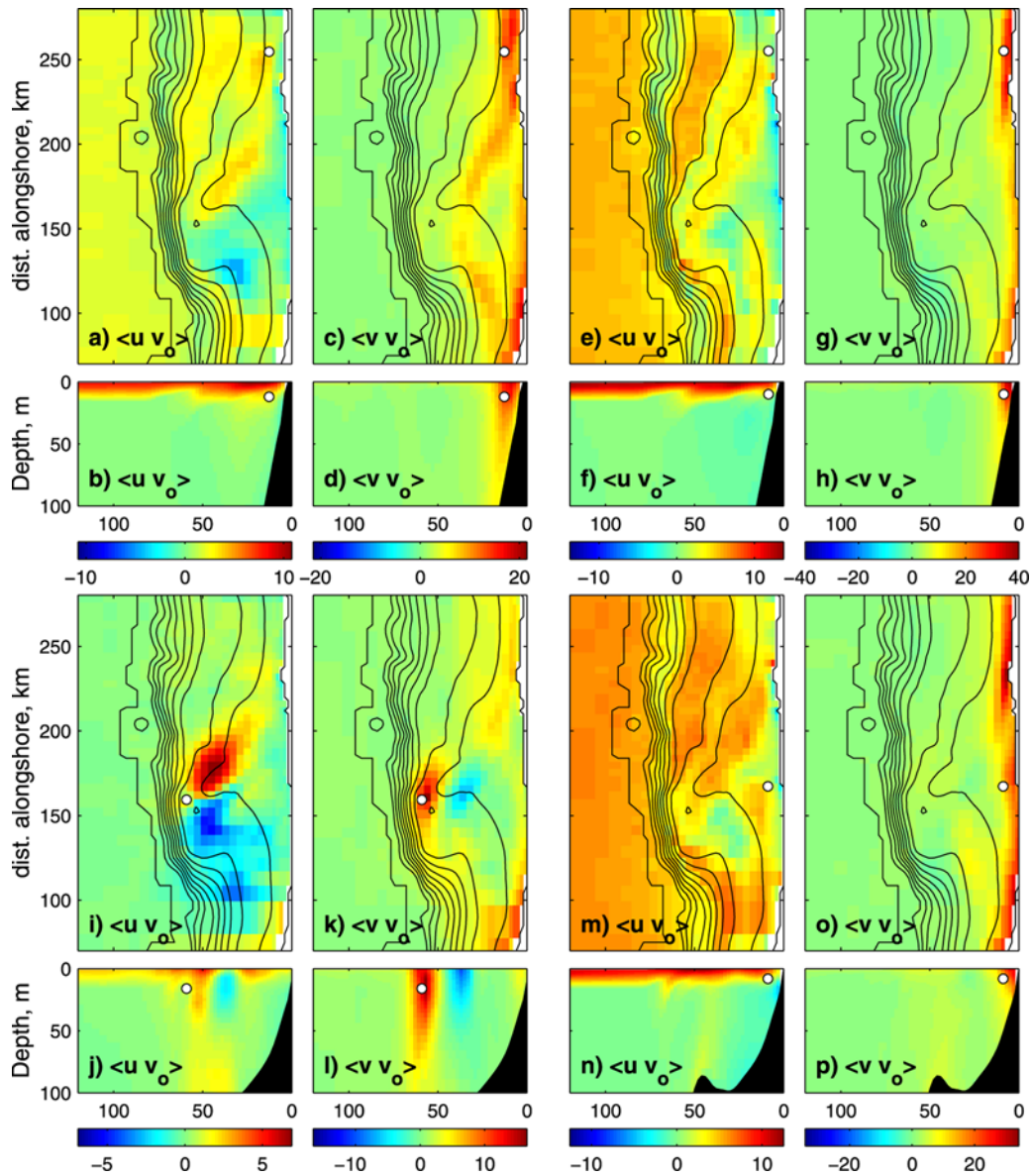


**Figure 10.** Horizontal and vertical cross-shore sections of the forecast error covariance  $\mathbf{P}^f \mathbf{H}^f$  ( $\text{cm}^2 \text{s}^{-2}$ ) corresponding to the  $v$  observation at the upper profiler bin of moorings: (a–d) NMS, at 12 m depth; (e–h) NIS, at 10 m; (i–l) SSB, at 16 m; and (m–p) SIS, at 8 m. The horizontal and cross-shore sections are through observation locations. Plots in columns 1 and 3 show  $u$ - $v$  covariances, and columns 2 and 4 show  $v$ - $v$  covariances. Horizontal coordinates show the distance from the coast (km).

linear) model [e.g., *Bennett*, 2002, chap. 1]. In Figure 9 a characteristic corresponding to southward advection is most apparent, indicated by the nearly vertical dashed line. Northward propagating coastal trapped waves (CTWs; suggested by the more horizontal line in Figure 9) are a dominant feature in the idealized analytical coastal representative model of *Kurapov et al.* [2002], but these waves do not have a clear manifestation in the lagged correlation, for a number of reasons. First, the most energetic CTWs propagate with speeds exceeding  $100 \text{ km d}^{-1}$  [*Brink*, 1991] and our periodic channel domain is too short (350 km) to see them clearly over large distances. Also, the limited-area periodic channel does not support CTWs with large alongshore scales.

[30] Each column of  $\mathbf{P}^f \mathbf{H}^f$  can be plotted as a 3-D, multivariate field. In Figure 10, we show the velocity components of these fields in horizontal and vertical cross-shore sections through the observation location for the columns corresponding to  $v$  measurements at four mooring sites. Sites NMS and SSB are chosen since they are closest to the core of the modeled upwelling jet; the two other sites are the near-shore NIS and SIS. In horizontal section plots of  $v$ - $v$  covariances (Figures 10c, 10g, 10k, and 10o) alongshore spatial scales are larger than cross-shore scales. The  $v$  errors are positively correlated with  $u$  errors in the surface Ekman layer, as best seen in cross-shore vertical sections (Figures 10b, 10f, 10j, and 10n). The  $v$ - $v$  covariance corresponding to the measurement at NMS (Figure 10c)

shows larger covariability in the direction of the upwelling jet, deflected from the coast. In the covariance corresponding to the measurement at SSB (Figures 10i, 10j, 10k, and 10l) short horizontal scales are introduced by bathymetry. In the vertical cross sections the maximum of  $v$ - $v$  covariance corresponding to the inner-shelf observation locations (Figures 10h and 10p) is closer to the shore and the surface than the observation point, consistent with an analytical representor solution [Scott *et al.*, 2000]. However, in horizontal sections covariances for NIS and SIS (Figures 10g and 10o) look suspicious because they have large alongshore scales and are confined near the coast. An artificially large alongshore correlation scale may result from the local response in shallow water to the spatially uniform winds used in the ensemble of solutions.

[31] In the work of Oke *et al.* [2002a], a time-distributed averaging procedure was designed to overcome issues of data compatibility and initialization, which made the algorithm more complicated than the concept expressed by (2). In particular, a low-pass filtered forecast was matched to low-pass filtered observations. We employ a faster scheme that was found to yield results of the same accuracy. In our implementation, the model is integrated forward from  $t = 0$  to  $t = 1/4 T_I$ , where  $T_I$  is the inertial period. The correction term is based on the difference of the low-pass filtered data and the instantaneous forecast at  $t = 1/4 T_I$ . Then, the model is restarted at  $t = 0$  and correction is imposed incrementally over a quarter of  $T_I$  so that by  $t = 1/4 T_I$  the full correction has been added. Then the whole process is repeated from  $t = 1/4 T_I$  to  $t = 1/2 T_I$ , and so on. Matching the filtered observations to the instantaneous model output (instead of low-pass filtered output) probably works because care is taken to avoid excitation of high-frequency modes in the solution by the use of low-pass filtered forcing variables.

[32] In this study, the data error covariance  $\mathbf{C}_d$  is taken to be equal to  $\sigma_d^2 \mathbf{I}$ , where  $\mathbf{I}$  is the identity matrix. We choose  $\sigma_d = 0.1 \text{ m s}^{-1}$ . The measurement error for the moorings is expected to be smaller. However,  $\mathbf{C}_d$  should also account for the error in  $\mathbf{H}$ , mapping the data to the state vector. For instance, since the model bathymetry is smoothed, mooring locations in the model have to be moved to points with the appropriate bottom depth, equal to the depth of actual mooring sites. To examine solution sensitivity to the data error variance, data assimilation computations have been performed for a range of  $\sigma_d$ . Computations with  $\sigma_d$  in the range from 0.05 to  $0.15 \text{ m s}^{-1}$  produce results of similar quality. When data are assimilated with a very low value  $\sigma_d = 0.01 \text{ m s}^{-1}$ , the analysis is fit too closely, and data error not consistent with the dynamics is assimilated into the model, reducing solution quality.

## 5. Distant Effect of Assimilating Currents From a Line of Moorings

[33] In this section we describe two series of experiments in which moored currents are assimilated from either the northern or the southern across-shore mooring line. The results are verified by comparison to velocity data from the moorings not used for assimilation. In the first series of experiments, data from the inner shelf is omitted because of concerns that the columns of  $\mathbf{P}'\mathbf{H}'$  corresponding to the inner-shelf sites reflect artificially long alongshore scales

(Figures 10g and 10o). In the second series data from the inner shelf moorings are added.

[34] Since a large fraction of the velocity variability is described by the depth average and the shear (see Figure 8), measurements of  $u$  and  $v$  from only four equally spaced acoustic profiler bins (Table 1) are assimilated (the uppermost, lowest, and two in between). To check sensitivity to the number of assimilated bins, experiments involving assimilation of the currents from 7 bins distributed evenly in the vertical were performed for comparison. Those yielded results very similar to the cases with four bins.

[35] For brevity, different data assimilation cases presented below will be referred to by the mooring sites from which data are assimilated, e.g., case DA (NSB+NMS) means data from the two northern moorings are assimilated and DA (Line N) means the data from all three moorings of the line are used.

[36] In case DA (NSB+NMS), we first compare the variance ellipses for the modeled and observed depth-averaged currents and see improvement at NH10 and SSB (Figure 7b). The model mean current at SSB, although reduced, remains too large. Time series of depth-averaged alongshore currents at NH10 and the moorings of Line S are shown in Figure 11. Model-data velocity rms errors and complex correlation amplitudes calculated for days 146–191 are given in Table 2. At NH10, which is only 40 km away from the assimilation site, improvement is obtained for the whole 91 day analysis period. At SSB, sensible improvement only occurs for days 146–191 (Figure 11). For days 191–237, there is some improvement in variability at this site, but the current is still much too large. No improvement is obtained at the SMS or SIS, although at the SIS accuracy in terms of rms error and correlation remains reasonably good.

[37] In Figure 12, model-data error statistics for case DA (NSB+NMS) are shown as a function of depth for each mooring. Improvement at the NIS, SSB, and NH10 is present throughout the water column, both in terms of rms error and correlation. At these sites, the phase angle of the complex correlation, which contains information about the difference in orientation of the velocity vectors, is below  $20^\circ$  except close to the surface at the SSB.

[38] In case DA (SSB+SIS), the modeled and observed mean depth-averaged currents at SSB are now close, since the model is fit to the data at this site (Figure 7c). At the SMS, the predicted variance is smaller than observed, despite data being assimilated here. Data assimilation improves the variance of the depth-averaged current at NH10, 50 km upstream from the assimilation site. At the moorings of Line N variance ellipses remain exceptionally good. At the same time, data assimilation reduces the magnitude of the mean current at the distant validation sites more than necessary. Comparison of the observed and modeled velocity time series shows improvement in terms of the model-data rms error and correlation at Line N and NH10 (Figure 13, and Table 2). Compared to the case of no DA, improvement is obtained throughout the water column (Figure 14), except for the rms error close to the surface at NMS and NIS. At the same time, the model data correlation is improved there.

[39] At the surface, DA reduces the time-averaged current and the vorticity  $\zeta$  on the inshore side of the upwelling jet

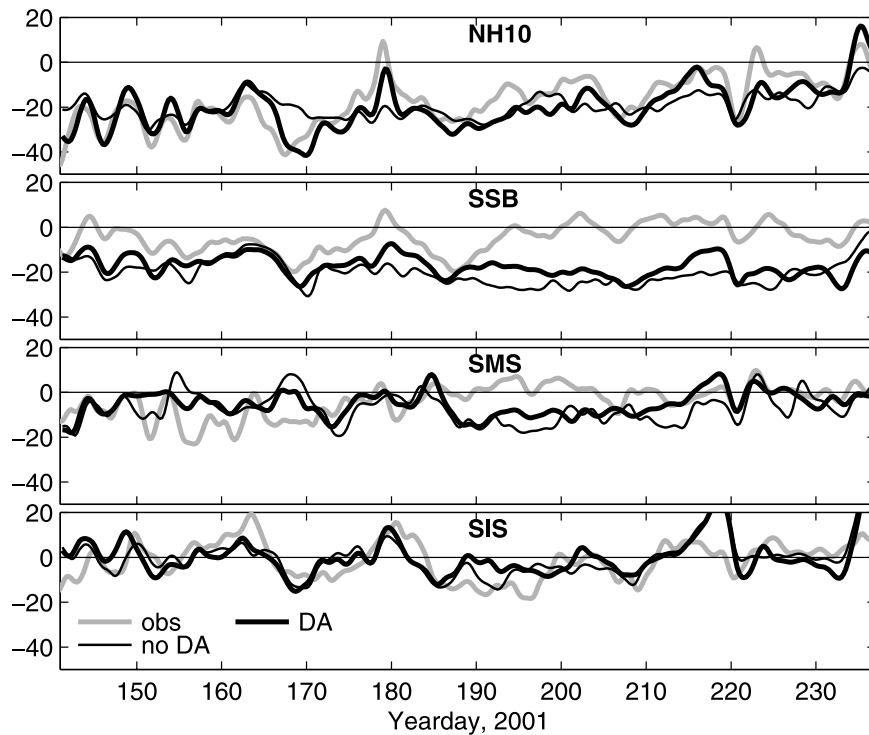


**Figure 11.** Time series of depth-averaged alongshore current ( $\text{cm s}^{-1}$ ) at the four mooring locations, NH10 and Line S. Solution DA (NSB+NMS) is the bold solid lines, the model solution without DA is the thin solid lines, and validation data are the shaded lines. Statistical comparisons are recorded in Table 2.

(Figures 3b and 3c). The variance in  $\zeta$  is not affected as much (Figures 3e and 3f). In case DA (NSB+NMS) mean depth-integrated transport streamlines are not affected significantly by data assimilation (Figure 3e). In case DA (SSB+SMS), the transport streamlines (Figure 3f) indicate that the jet is closer to the coast than in the model-only case, especially over, and to the south of Heceta Bank. However, at the same time the modeled mean depth-averaged current vector at NH10 is directed less offshore than the corresponding observation (see Figure 7c). Figure 3f also suggests that assimilation of data from Line S has a strong smoothing effect on the flow field in the region directly south of that line. This issue is addressed in our follow up manuscript [Kurapov *et al.*, 2005].

[40] In both DA cases described above, the model constrained by the data fails to reproduce the patches of cold water extending offshore that are seen in the satellite SST images during the second part of the study period (see Figures 6c and 6d). This is in spite of the fact that in case DA (SSB+SMS) the model is fit to the velocity data at the SSB. In section 3 we hypothesize that this separation may be influenced by remote forcing. In the present model setup data assimilation does not change the nature of the boundary conditions at the south boundary relative to that at the north boundary and the analysis solution remains periodic in the alongshore direction. Unless the boundary is open, data assimilation is not effective in reducing the solution error associated with remote forcing.

[41] Analysis of terms in the depth-averaged momentum equation allows us to check how large the DA correction is

and to see if dominant term balances are preserved. In Figure 15, time-averaged dynamical balances are shown in the area between the moorings of Line N and of Line S. The upper plots correspond to the model without DA, and the lower plots are for case DA (SSB+SMS). To better represent the alongshore direction of the mean flow, the terms are projected onto the approximate direction of the upwelling jet, indicated by the offshore slanting direction of the longer side of the box surrounding the analyzed area. Shown in the figure are the ageostrophic (the Coriolis and pressure gradient terms combined), horizontal advection, surface and bottom stress, and the DA correction terms all written on the left hand side of the equation. The time-averaged tendency term is close to zero and is not shown. The contribution of the horizontal viscosity term to the dynamical balances is small on the shelf [Oke *et al.*, 2002a] and this term is added to the nonlinear advection term, for completeness. The main balance in the model is between the ageostrophic and nonlinear terms. Qualitatively, this balance is preserved in the DA solution, though both terms are reduced in amplitude. The time-averaged correction term has the same sign and magnitude as the bottom stress, and this tends to reduce the southward current. Assimilation of the currents at Line S provides a large scale correction, smooth in the vicinity of the data sites. Similar conclusions are reached based on analysis of case DA (NSB+NMS) (not shown).

[42] Adding the data from NIS to the assimilation set NSB+NMS does not have a significant impact on results (compare rows in Table 2 corresponding to cases NSB+NMS and Line N). This suggests the data from mooring NIS is redundant with data from nearby sites NSB and NMS. Indeed,

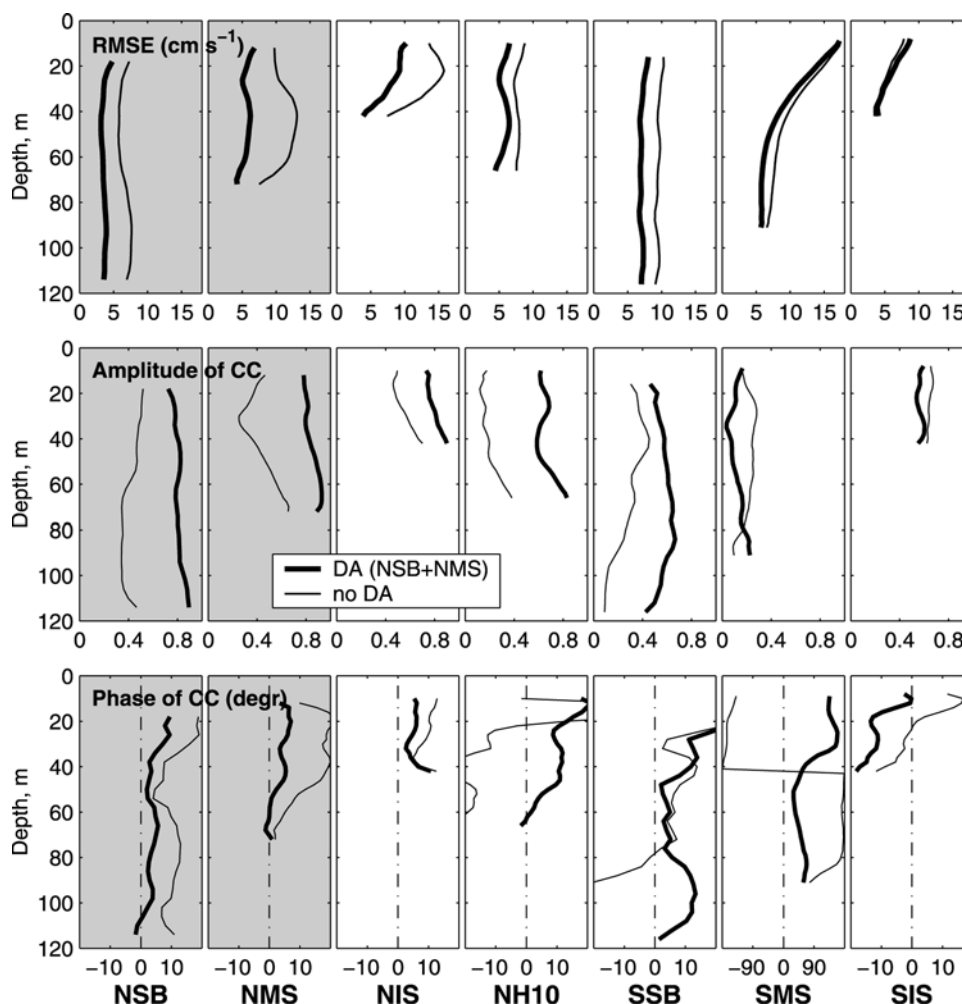


**Figure 12.** Model data velocity statistics versus depth at the seven mooring sites for the model-only solution (thin lines) and DA (NSB+NMS) (bold lines) for days 146–191: (top) rms error and the (middle) amplitude and (bottom) phase of the complex correlation coefficient. Each column of plots corresponds to a mooring. Plots on the shaded background are for the assimilated sites.

case DA (NSB+NMS) provides significant improvement at NIS (see Figure 12). If currents from the SIS are assimilated together with data from SSB and SMS, performance at Line N, especially at the mid- and inner-shelf, is worse than in case DA (SSB+SMS) (compare rows in Table 2 corresponding to cases SSB+SMS and Line S). This supports our inference that  $\mathbf{P}'$  corresponding to the inner-shelf data is not reasonable in the far field. However, at the same time, at NH10, case DA (Line S) yields better results than case DA (SSB+SMS). Thus the DA system does recover useful information from SIS to constrain the solution near NH10 in the separation zone inshore of the upwelling jet.

[43] Comparison of model-only and data assimilation solutions suggests that the forecast may be biased, predicting on average a larger southward current than observed. Vertical profiles of time-averaged differences between observed and forecasted alongshore velocities for days 146–191 are plotted in Figure 16 (solid lines) for cases DA (NSB+NMS) (plots a and b) and DA (SSB+SMS) (plots c and d). Dashed lines in these plots show 95% confidence limits for the means, assuming 15 degrees of freedom in the

45 day low-pass filtered time series [see *Oke et al.*, 2002a]. If data errors are assumed to be unbiased, the bias in the data forecast differences must be attributed to the forecast bias. On the path of the upwelling jet, at NMS [in case DA (NSB+NMS)] and at SSB (in case DA (SSB+SMS)), the positive bias is statistically significant in the lower part of the water column. One possible source for the forecast bias may be insufficient horizontal resolution that does not allow short scale (8–10 km) frontal instabilities to develop. These instabilities are found, e.g., in the 1 km resolution model of *Durski and Allen* [2005]. As a result, the upwelling current in the coarse resolution model may be larger because energy is not lost to small scale fluctuations and eddies. To compensate for this deficiency, data assimilation introduces a large scale correction of the same sign as the bottom drag. Other possible sources for the forecast bias are improperly represented large scale pressure gradients and insufficient form drag over smoothed model bathymetry.

[44] We attempted to correct the forecast bias sequentially, following the approach of *Dee and da Silva* [1998]. This approach requires specification of a statistical model for the

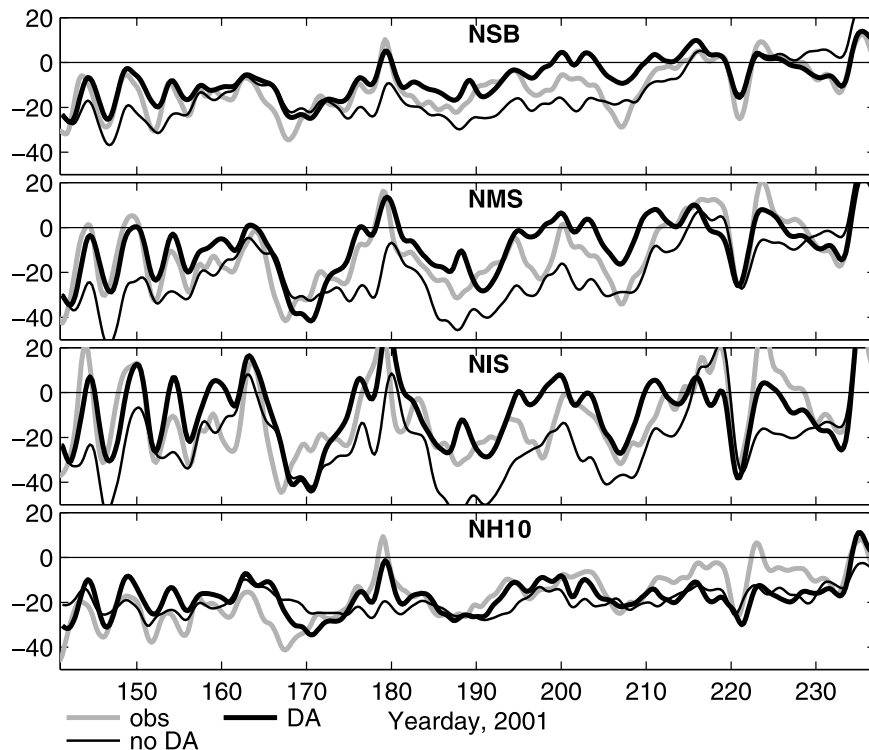


**Figure 13.** Time series of depth-averaged alongshore current ( $\text{cm s}^{-1}$ ) at four mooring locations, Line N and NH10. Solution DA (SSB+SMS) is the bold black lines, the model solution without DA is the thin black lines, and validation data are the shaded lines. Statistical comparisons are recorded in Table 2.

bias, including a bias prediction error covariance. Since we do not have enough information for an informed choice of such a covariance, we tried a covariance proportional to  $\mathbf{P}^f$  following *Dee and da Silva* [1998]. Unfortunately, accounting for the bias in this way did not help to improve the solution quality compared to the DA cases based on the bias-free statistical model and these efforts were abandoned.

## 6. Assimilation of Currents From a Single Mooring

[45] It is uncommon to have current profiles from as many as 7 moorings available in a coastal area spanning 100 km alongshore. To guide the design of a cost effective coastal observing system, it is important to know how well the model circulation is constrained by data from a smaller set of moorings and what the best placements for these moorings should be. In the previous section we have shown that the use of two moorings on a cross-shore line provides useful corrections at a distance of 90 km along the jet path (both upstream and downstream). It has also been shown that in some cases additional data do not bring extra benefits or, if model covariances are not accurately specified, may even reduce the accuracy of the prediction.

[46] In this section we investigate the net effect of assimilation of data from only one mooring. The model data error statistics for these 7 cases are given in Table 2. Some of the conclusions from this table are that case DA (NMS) provides solutions at NH10 and SSB with accuracy very close to case DA (NSB+NMS). Case DA (NIS) also performs well at those validation sites, although results at SIS are not as good as in case DA (NMS), both in terms of

rms error and model data correlation. Note that in case DA (NIS) improvement is attained at the SSB, although the forecast error covariance of velocities at the NIS and SSB is small (see Figure 10g). At the same time, case DA (NIS) makes the solution at SIS significantly worse than the model-only prediction. This reduction in the solution quality evidently is associated with the artificially large alongshore scale of the forecast error covariance. Quite surprisingly, even though DA (Line N) does not result in large gains to the solution quality at SMS, assimilation at the SMS alone, where the flow variability is not strongly correlated with the wind stress, yields improvement at the sites of Line N of about the same magnitude as that in case DA (SSB). Assimilation of data from the SSB or SMS appears to be more useful for the analysis in the northern part of the domain than at nearby sites of Line S. Finally, solution DA (SIS) is worse than the model solution everywhere away from the assimilation site.

[47] For the cases involving assimilation of data from one mooring we compare the actual and expected error variance improvement resulting from DA. Such a comparison provides a consistency test of our statistical hypothesis about errors in the forecast and data. In particular, it provides additional indications of the deficiency of the forecast error covariance for inner-shelf data.

[48] The actual improvement (AI) in the model data error variance is computed as

$$\text{AI} = \text{RMSE}_m^2 - \text{RMSE}_a^2, \quad (6)$$

where RMSE is the model data rms error (1) with respect to a chosen validation data set, and indices  $m$  and  $a$  stand for

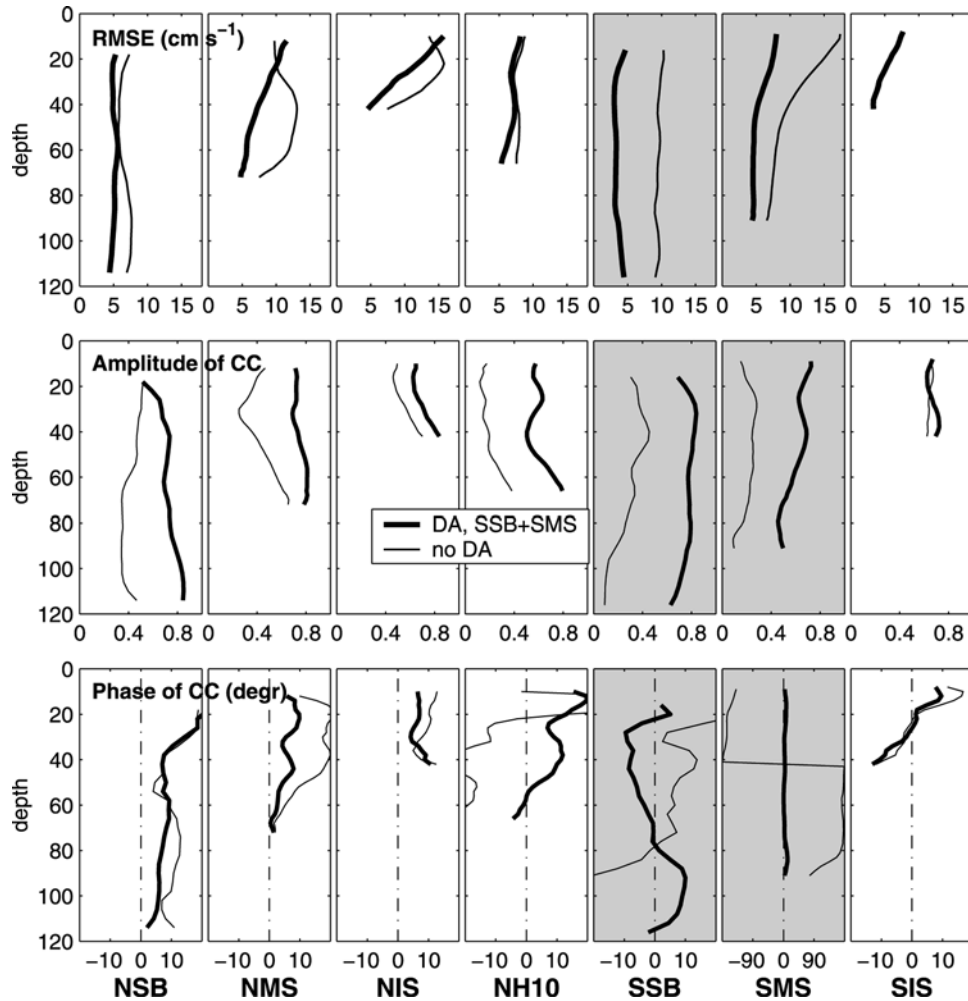


**Figure 14.** Model data velocity statistics versus depth at the seven mooring sites for the model-only solution (thin lines) and DA (SSB+SMS) (bold lines): (top) rms error, (middle) the amplitude, and (bottom) the phase of the complex correlation coefficient. Each column of plots corresponds to a mooring. Plots on the shaded background are for the assimilation sites.

the model-only and analysis solutions, respectively. Note that in our case RMSE computation involves depth averaging of squared model data differences. The expected improvement (EI) in the error variance is computed given the assumptions about the model and data errors. In general terms, the diagonal elements of the model error covariance  $\mathbf{P}_{t,t}^m$  should be compared with those of the analysis covariance matrix  $\mathbf{P}^a$  [e.g., *Miller and Cane, 1989*]:

$$\mathbf{P}^a = \mathbf{P}^f - \mathbf{GHP}^f. \quad (7)$$

Note that in the RMSE computation (1) the model (or analysis) solution is compared to the data time series, whereas in the definition of  $\mathbf{P}^m$  and  $\mathbf{P}^a$  the solution is matched to the (unknown) truth, rather than the data. To make EI comparable to AI (6), it should also be computed based on the difference of the model-data and analysis-data error variances, rather than model-truth and analysis-truth error variances. An analysis that provides a relevant expression for EI is given in Appendix A.

[49] Comparisons of the actual and expected improvements in the model data error variance, utilizing (6) for AI

and (A3) for EI, are shown graphically in Figure 17. The areas of the circles in this graph are proportional to the magnitude of variance improvement; clear (black) circles are for positive (negative) values. Each row corresponds to a DA case, and columns to the validation sites. For each validation site, the left and right columns correspond to AI and EI, respectively. In positions corresponding to EI at the assimilation sites, where two concentric circles are plotted, the inner circle shows the magnitude of the first term in (A3). Except for NH10 and SIS, the effect of the second term in (A3) is to bring EI in closer agreement with AI.

[50] The actual effect of assimilating data from NSB, NMS, NIS, or NH10 is comparable to the expectation when evaluation is done at the same group of sites. For instance, compare the general similarity in AI and EI for these four sites in the upper left corner of Figure 17. At the same time, as a result of assimilation of data from one of these four moorings, the actual improvement is larger than the expectation at SSB. In each of these four cases the AI is negative at SIS.

[51] The most striking discrepancy is between the actual and expected improvement in case DA (SIS). At the

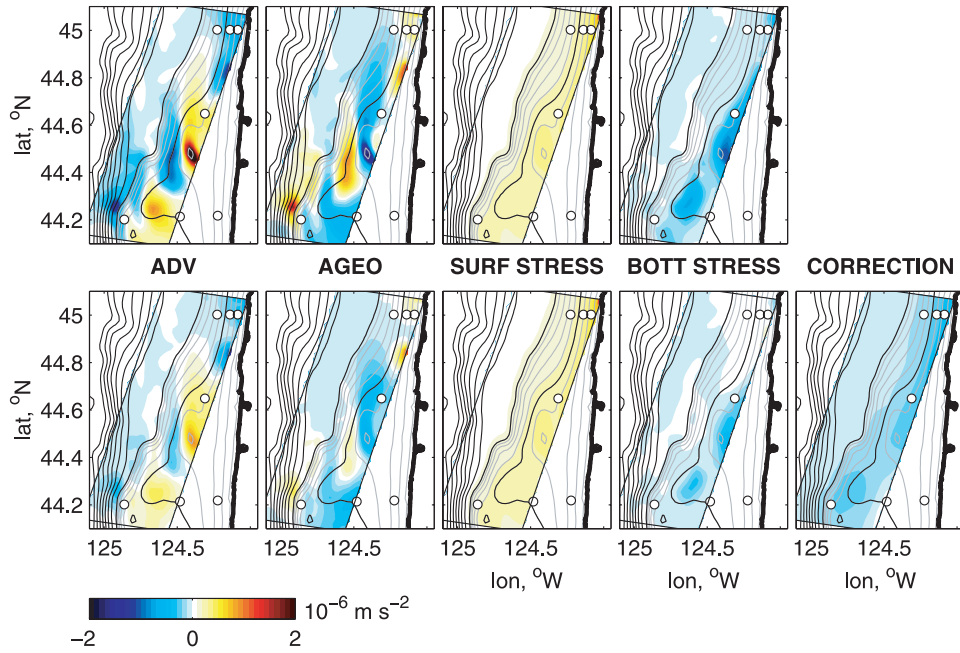


**Figure 15.** Terms in the time- and depth-averaged momentum equations projected onto the approximate direction of the upwelling jet (the direction of projection coincides with the orientation of the longer side of the border surrounding the analysis area). (top) Model-only solution. (bottom) DA (SSB+SMS). From left to right, plots are advection plus horizontal diffusion, ageostrophic (sum of the Coriolis force and the pressure gradient terms), surface stress, bottom stress, and DA correction terms. The time-averaged tendency term (not shown) is close to zero in both cases.

moorings of Line N, NH10, and SSB the analysis solution is significantly worse than the model-only solution, contrary to our expectations. The actual improvement at the assimilation site is significantly smaller than the expectation, in contrast to all the other sites. Note that from the statistical perspective the average improvement should never be negative, so the negative values of AI indicate a problem with the statistical hypotheses assumed in the data assimilation method. We think that the instances where the actual improvement is negative arise from the erroneously long

spatial scale of  $\mathbf{P}^f$  in shallow water, as previously discussed in connection with Figure 10. Thus  $\mathbf{P}^f \mathbf{H}^f$  corresponding to the inner-shelf locations should be reevaluated to make better use of this data.

## 7. Role of Propagating Modes

[52] Correction at a distance from the assimilation site may be applied instantly if the scale of the forecast error covariance is large enough, or may be built up gradually as

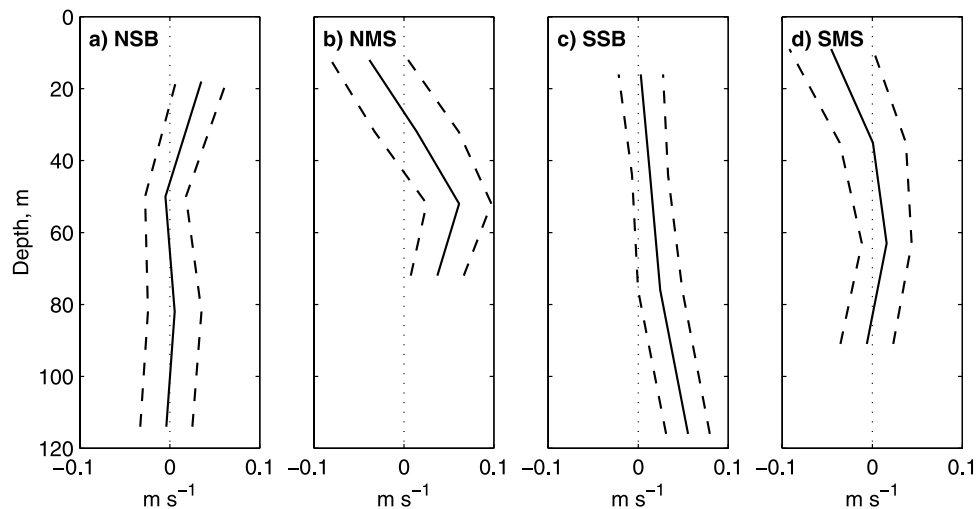


**Figure 16.** Alongshore velocity data forecast differences at assimilation sites, (a, b) cases DA (NSB+NMS) and (c, d) DA (SSB+SMS). The solid line is the time average, and dashed lines show the 95% confidence limits.

Cases	Validation sites											
	NSB		NMS		NIS		NH10		SSB		SIS	
	AI	EI	AI	EI	AI	EI	AI	EI	AI	EI	AI	EI
NSB	○	○	○	○	○	○	○	○	○	○	○	○
NMS	○	○	○	○	○	○	○	○	○	○	○	○
NIS	○	○	○	○	○	○	○	○	○	○	○	○
NH10	○	○	○	○	○	○	○	○	○	○	○	○
SSB	○	○	○	○	○	○	○	○	○	○	○	○
SMS	○	○	○	○	○	○	○	○	○	○	○	○
SIS	●	○	●	○	●	○	●	○	●	○	○	○

**Figure 17.** Actual AI and expected EI improvement in the model data error variance resulting from assimilation of currents from only one mooring. Rows in the table correspond to different DA cases, and columns correspond to evaluation sites. Empty circles mean positive improvement, and filled circles mean that the DA model data error variance is worse than that of the model-only solution. The magnitude of the improvement is proportional to the area of a circle (e.g.,  $28.1 \text{ cm}^2 \text{ s}^{-2}$  for the circle in the upper left corner). Inner circles in positions with two concentric circles show the magnitude of the first term in (A3).

a result of dynamical adjustment. For instance, in our case corrections introduced near the data site may be advected to the south with the upwelling jet. This in part explains why assimilation of currents at Line N positively affects the solution at NH10 and especially at SSB, which is separated by a distance exceeding the scale of the implied forecast error covariance in that direction (e.g., see Figure 10c). At the same time, there was limited or no improvement on the inshore side of the upwelling jet in the separation zone near Heceta Bank. Representer solutions for linear coastal models suggest that corrections can be propagated with the free modes of the dynamical model [Kurapov *et al.*, 2002, 2003]. As noted in section 4, coastal trapped waves propagating to the north are difficult to detect in the model solutions obtained in a short periodic channel. So the reasons for improvement to the north of the assimilation site, taking into account the relatively short spatial scales of  $\mathbf{P}^f$  corresponding to SSB (see Figures 10i and 10k), remain an open question, but presumably are related to the dynamical effects associated with coastal trapped waves. Representer computations using the tangent linear and adjoint codes, when those become available, may provide new insights into that issue.

[53] A better understanding of the role of propagating dynamical modes in data assimilation would help in designing a coastal observing system, to optimize deployment of a small set of instruments that most effectively improve the model predictions. Some of the basic effects of the propagating modes relevant to OI, for instance their effect on the spatial structure of the forecast error covariance, can be illustrated in a model based on the simple wave equation

$$\frac{\partial u}{\partial t} + c \frac{\partial u}{\partial y} + \alpha u = \phi(y, t) + \epsilon(y, t), \quad (8)$$

subject to the initial condition

$$u(y, 0) = 0. \quad (9)$$

In (8), the scalar  $u$  is a function of the coordinate  $y$  ( $-\infty < y < +\infty$ ) and time  $t$ , the constant  $c$  is the wave speed,  $\alpha$  is the dissipation parameter,  $\phi(y, t)$  is the deterministic forcing, and  $\epsilon(y, t)$  is the random forcing error. In an idealized sense, equation (8) may be considered a conceptual model describing either dynamics of long coastal trapped waves [Brink, 1991] or advection by the background current. The forcing error is assumed to be unbiased with a covariance implying that errors are correlated in space, but not in time:

$$\langle \epsilon(y_1, t_1) \epsilon(y_2, t_2) \rangle = \delta(t_1 - t_2) C(y_1 - y_2). \quad (10)$$

The solution to (8)–(9) is obtained by integration along characteristics. The prior model solution  $u^m(y, t)$  is obtained for  $\epsilon = 0$ . If  $t$  and  $t_o$  are large compared to the dissipation time scale  $\alpha^{-1}$ , the covariance of the errors in the prior model solution  $\delta u^m(y, t) = u^m - u$  is [e.g., Miller and Cane, 1989]

$$\begin{aligned} P^m(y, t; y_o, t_o) &\equiv \langle \delta u^m(y, t) \delta u^m(y_o, t_o) \rangle \\ &\approx \frac{e^{-\alpha|t-t_o|}}{2\alpha} C[y - y_o - c(t - t_o)]. \end{aligned} \quad (11)$$

Thus after a long enough integration time,  $P^m$  becomes stationary. The lagged covariance ( $t \neq t_o$ ) is obtained by translation of a scaled shape  $C(y - y_o)$  along the  $y$  axis.

[54] We utilize (11) to compute the forecast error covariance (4) assuming  $u$  data are assimilated sequentially every 4 hours at  $y = 0$ , the forcing error covariance function is  $C = \exp[-(y - y_o)^2/l^2]$ , where  $l = 50 \text{ km}$ , the data error covariance is  $\mathbf{C}_d = 0.01 \mathbf{I}$ , and  $\alpha = 1/5 \text{ d}^{-1}$ . The forecast error covariance  $\mathbf{P}^f \mathbf{H}^T$  is shown in Figure 18 for two different cases  $c = 30$  and  $100 \text{ km d}^{-1}$  (dashed and solid bold lines, correspondingly). As an effect of the data previously assimilated in the wave model (8), the optimum forecast error covariance is asymmetric with respect to the observation location  $y_o$ , with a shorter spatial scale in the direction of wave propagation, even though  $P^m(y, t; y_o; t)$  is symmetric with respect to  $y_o$  (thin line in Figure 18).

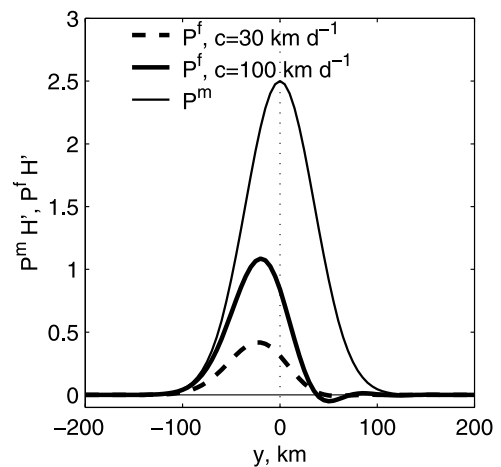


**Figure 18.** Prior model and forecast error covariance of  $u(y)$  and  $u(y_o)$  for the model based on the wave equation (8) assuming that  $u$  data are assimilated sequentially at  $y_o = 0$  every 4 hours,  $t = 40$  days. The free wave propagates in the direction of positive  $y$  values.

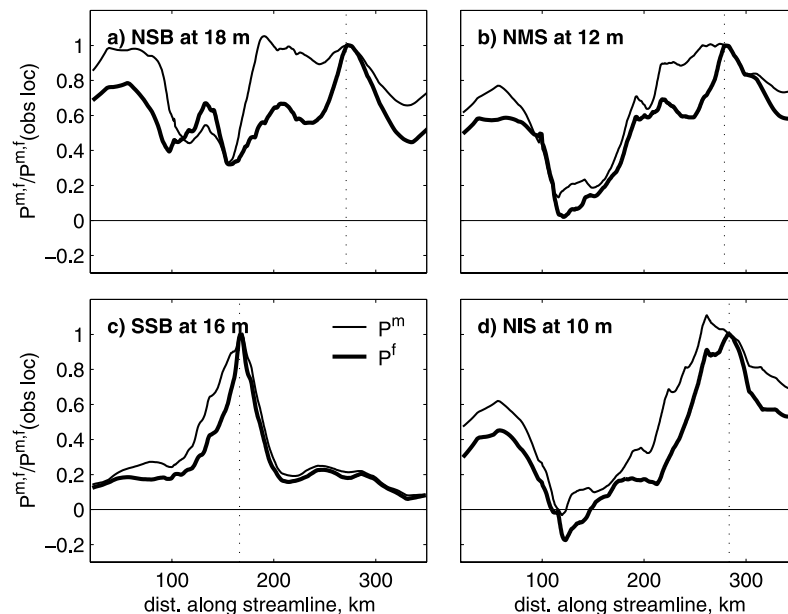


**Figure 19.** Model-only (thin lines) and forecast error (bold lines) covariances of the tangential velocities  $v_\tau$  at the observation location (dotted vertical line) and points taken at the same depth along the mean depth-integrated transport streamline through the observation point. Covariances are normalized by their value at the observation location to highlight the difference in spatial scales. Measurement sites are (a) NSB at 18 m; (b) NMS at 12 m; (c) SSB at 16 m; and (d) NIS at 10 m.

[55] Some of the effects obtained with the wave equation are common to our oceanographic case. A propagating feature corresponding to advection is seen in the estimate of lagged model correlations (Figure 9). Also, plotted along the transport streamline at the depth of observation point,  $\mathbf{P}^f$  for the tangential velocities along the streamline has shorter spatial scales than  $\mathbf{P}^m$  (Figure 19) particularly evident to the south from the observation site, in the direction of the mean alongshore advection.

## 8. Summary

[56] Sequential OI-based assimilation of depth-dependent current measurements into a coastal circulation model shows that data from one or two moorings provides significant improvement in the velocity prediction along the path of the upwelling jet at an alongshore distance of 90 km, both downstream (in the direction of advection) or upstream (in the direction of CTW propagation). Where the jet is deflected from the coast, additional velocity mooring installations may be necessary to constrain the solution in the inshore separation zone.

[57] The choice of the forecast error covariance may be critical for efficient use of the data. An artificially long spatial scale for the covariance corresponding to inner-shelf sites resulted here from the spatially constant wind forcing used in the calculation of  $\mathbf{P}_{s,q}^m$ . With such a forecast error covariance, the use of inner-shelf data does not increase accuracy of predictions at a distance of 90 km. Assimilation of currents at SIS in addition to SSB+SMS actually reduces the quality of predictions at Line N. For predictions at a closer distance (NH10) inclusion of SIS data is beneficial. In experiments where data from only one mooring are assimilated, comparison of the actual and expected DA

performance provides a consistency test for the  $\mathbf{P}^f$ , and further demonstrates the need for an improved forecast error covariance for inner-shelf locations.

[58] The analysis of the wave equation shows that propagating dynamical modes affect the spatial structure of  $\mathbf{P}^f$ , shortening decorrelation length scales of  $\mathbf{P}^f$  in the direction of propagation compared to  $\mathbf{P}^m$ , the model error covariance unconstrained by previously assimilated data. A similar effect is evident in the direction of southward advection in the covariances applied here with the ocean circulation model. At alongshore distances from the data sites greater than the length scales implied by  $\mathbf{P}^f$  the correction to the model solution can be a result of dynamical adjustment.

[59] The accuracy of our solutions constrained by the velocity data is better for the first part of our study period (days 141–190). Analysis of satellite SST images raises concerns about the adequacy of our limited area model for the later part of the study period. It is possible that flow behavior in the area offshore of the mooring installations is coupled dynamically with separation of the upwelling jet off Cape Blanco, about 150 km to the south or with the poleward undercurrent [Huyer, 1983; Pierce *et al.*, 2000]. Neither of these processes are represented in our limited area model. To extend this study, a high-resolution open boundary model nested in a larger scale model should be implemented. Information passed from the larger scale model should be considered a prior guess with the data inside the domain used to reduce open boundary errors. In the context of a model based on the fully nonlinear primitive equations, such a task is more challenging than cases based on a quasi-geostrophic model [Yaremchuk and Maximenko, 2002] or on the linearized primitive equation model [Kurapov *et al.*, 2003]. For instance, a model like POM is sensitive to

specification of open boundary values owing to the fact that the continuous model based on inviscid hydrostatic primitive equations can be ill posed if the open boundary values are specified locally [Oliger and Sundström, 1978; Bennett, 2002, section 6.4]. Open boundary conditions implemented for our study region should allow outgoing waves to radiate freely and at the same time represent dynamic modes coming into the computation domain. For instance, at the northern end of our domain open boundary conditions should be radiative for outgoing coastal trapped waves and at the same time be receptive for incoming information advected into the area with a southward upwelling jet. Separation of the flow into incoming and outgoing parts is nontrivial over realistic bathymetry. Some progress in this direction is reported by Dinniman and Klink [2002] and Gan and Allen [2005]. The use of data assimilation for open boundary flow correction brings additional problems. For instance, the choice of an open boundary error covariance affects wave radiation and ultimately solution quality inside the domain [see Kurapov et al., 2003].

[60] The forecast error in the interior of the computational domain may result from imperfect open boundary values from earlier times that have been advected inside the domain. To provide correction to the open boundary values back in time using present data in the interior, variational (smoothing) methods rather than filtering should be employed. Variational methods are also capable of providing, where appropriate, a dynamically balanced solution such that the effect of DA on term balances can be investigated. New methods and tools [e.g., Chua and Bennett, 2001; Moore et al., 2004] should be tested for this use. The present study, showing the positive effect of assimilation of currents from moored acoustic Doppler profilers at a substantial alongshore distance, suggests that these data would contain important information about boundary values in an open boundary implementation.

## Appendix A: Expected RMSE Improvement

[61] In the formal derivation here we use linear algebra notation. Lower and upper case bold symbols stand for vectors and matrices, respectively, and the prime denotes matrix transpose. The errors in the model-only solution, forecast, and the analysis are  $\mathbf{e}_{\{m,f,a\}} = \mathbf{w}^{\{m,f,a\}} - \mathbf{w}$ , where  $\mathbf{w}$  denotes the true state. Then,  $\mathbf{P}_{t,t}^m = \langle \mathbf{e}_m \mathbf{e}_m' \rangle$ ,  $\mathbf{P}^f = \langle \mathbf{e}_f \mathbf{e}_f' \rangle$ , and  $\mathbf{P}^a = \langle \mathbf{e}_a \mathbf{e}_a' \rangle$ , where angle brackets denote ensemble averaging. The assimilation data set is defined by  $\mathbf{H}$  and  $\mathbf{d}$ , with the associated data error  $\mathbf{e}_d = \mathbf{d} - \mathbf{H}\mathbf{w}$ . The validation data set is defined by  $\mathbf{H}_1$  and  $\mathbf{d}_1$ , with errors in the validation data  $\mathbf{e}_1 = \mathbf{d}_1 - \mathbf{H}_1\mathbf{w}$ . The model data error covariance at the validation sites is

$$\langle (\mathbf{H}_1\mathbf{w}^m - \mathbf{d}_1)(\mathbf{H}_1\mathbf{w}^m - \mathbf{d}_1)' \rangle = \mathbf{H}_1\mathbf{P}_{t,t}^m\mathbf{H}_1' + \langle \mathbf{e}_1 \mathbf{e}_1' \rangle, \quad (\text{A1})$$

assuming  $\langle \mathbf{e}_1' \mathbf{e}_1' \rangle = 0$ , which is reasonable for a case of data errors uncorrelated in time. Taking into account (2), the analysis data error covariance is

$$\begin{aligned} \langle (\mathbf{H}_1\mathbf{w}^a - \mathbf{d}_1)(\mathbf{H}_1\mathbf{w}^a - \mathbf{d}_1)' \rangle &= \mathbf{H}_1\mathbf{P}^a\mathbf{H}_1' + \langle \mathbf{e}_1 \mathbf{e}_1' \rangle - \mathbf{H}_1\mathbf{G}\langle \mathbf{e}_d \mathbf{e}_d' \rangle \\ &\quad - \langle \mathbf{e}_1 \mathbf{e}_d' \rangle \mathbf{G}'\mathbf{H}_1'. \end{aligned} \quad (\text{A2})$$

The expected variance improvement EI is then the mean of the diagonal elements of (A1) minus (A2):

$$\text{EI} = \text{mean diag} \left\{ \mathbf{H}_1 \left( \mathbf{P}_{t,t}^m - \mathbf{P}^a \right) \mathbf{H}_1' \right\} + \text{mean diag} \left\{ 2\mathbf{H}_1\mathbf{G}\langle \mathbf{e}_d \mathbf{e}_d' \rangle \right\}. \quad (\text{A3})$$

In our implementation, data errors are assumed to be spatially uncorrelated. Then, if the data are assimilated at one mooring and EI is estimated at another mooring site, then the second term in (A3) is 0. If EI is assessed at the assimilation site, the second term in (A3) is reduced to evaluation of the mean of diagonal elements of  $2\mathbf{H}\mathbf{G}\mathbf{C}_d$ .

[62] **Acknowledgments.** This research was supported by the Office of Naval Research (ONR) Ocean Modeling and Prediction Program under grant N00014-98-1-0043, by the National Science Foundation (NSF) Coastal Ocean Processes (CoOP) program under grant OCE-9907854, and by the NSF GLOBEC Program under grant OCE-0000733. The satellite imagery in Figure 6 is courtesy of T. Strub, Oregon State University, with funding by the U.S. GLOBEC NEP project (NSF and NOAA). The authors thank Peter Oke for guidance on model implementation.

## References

- Allen, J. S., P. A. Newberger, and J. Federiuk (1995), Upwelling circulation on the Oregon continental shelf. Part I: Response to idealized forcing, *J. Phys. Oceanogr.*, *25*, 1843–1866.
- Beadsley, R. C., E. P. Dever, S. J. Lentz, and J. P. Dean (1998), Surface heat flux variability over the northern California shelf, *J. Geophys. Res.*, *103*, 21,553–21,586.
- Bennett, A. F. (2002), *Inverse Modeling of the Ocean and Atmosphere*, 234 pp., Cambridge Univ. Press, New York.
- Blumberg, A. F., and G. L. Mellor (1987), A description of a three-dimensional coastal ocean circulation model, in *Three-Dimensional Coastal Ocean Models*, *Coastal Estuarine Sci. Ser.*, vol. 4, edited by N. Heaps, pp. 1–16, AGU, Washington, D. C.
- Boyd, T., M. D. Levine, P. M. Kosro, S. R. Gard, and W. Waldorf (2002), Observations from moorings on the Oregon continental shelf, May–August 2001, *Ref. 2002-6, Data Rep. 190*, *Oreg. State Univ.*, Corvallis.
- Breivik, Ø., and Ø. Sætra (2001), Real time assimilation of HF radar currents into a coastal ocean model, *J. Mar. Syst.*, *28*, 161–182.
- Brink, K. H. (1991), Coastal-trapped waves and wind-driven currents over the continental shelf, *Annu. Rev. Fluid Mech.*, *23*, 389–412.
- Chen, C.-S., and D.-P. Wang (1999), Data assimilation study of the Santa Barbara Channel circulation, *J. Geophys. Res.*, *104*, 15,727–15,741.
- Chua, B. S., and A. F. Bennett (2001), An inverse ocean modeling system, *Ocean Modell.*, *3*, 137–165.
- Dee, D. P., and A. M. da Silva (1998), Data assimilation in presence of forecast bias, *Q. J. R. Meteorol. Soc.*, *124*, 269–295.
- Dinniman, M. S., and J. M. Klink (2002), The influence of open versus periodic alongshore boundaries on circulation near submarine canyons, *J. Atmos. Oceanic Technol.*, *19*, 1722–1737.
- Durski, S. M., and J. S. Allen (2005), Finite amplitude evolution of instabilities associated with the coastal upwelling front, *J. Phys. Oceanogr.*, in press.
- Federiuk, J., and J. S. Allen (1995), Upwelling circulation on the Oregon continental shelf. Part II: Simulations and comparisons with observations, *J. Phys. Oceanogr.*, *25*, 1867–1889.
- Fukumori, I. (2002), A partitioned Kalman filter and smoother, *Mon. Weather Rev.*, *130*, 1370–1383.
- Gan, J., and J. S. Allen (2005), On open boundary conditions for a limited-area coastal model off Oregon. Part I: Response to idealized wind forcing, *Ocean Modell.*, 115–133.
- Huyer, A. E. (1983), Coastal upwelling in the California Current system, *Prog. Oceanogr.*, *12*, 259–284.
- Kosro, P. M., J. A. Barth, and P. T. Strub (1997), The coastal jet: Observations of surface currents over the Oregon continental shelf from HF radar, *Oceanography*, *10*, 53–56.
- Kundu, P. K. (1976), Ekman veering observed near the ocean bottom, *J. Phys. Oceanogr.*, *6*, 238–242.
- Kurapov, A. L., G. D. Egbert, R. N. Miller, and J. S. Allen (2002), Data assimilation in a baroclinic coastal ocean model: Ensemble statistics and comparison of methods, *Mon. Weather Rev.*, *130*, 1009–1025.

- Kurapov, A. L., G. D. Egbert, J. S. Allen, R. N. Miller, S. Y. Erofeeva, and P. M. Kosro (2003),  $M_2$  internal tide off Oregon: Inferences from data assimilation, *J. Phys. Oceanogr.*, *33*, 1733–1757.
- Kurapov, A. L., J. S. Allen, G. D. Egbert, R. N. Miller, P. M. Kosro, M. Levine, T. Boyd, J. A. Barth, and J. Moum (2005), Assimilation of moored velocity data in a model of coastal wind-driven circulation off Oregon: Multivariate capabilities, *J. Geophys. Res.*, doi:10.1029/2004JC002493, in press.
- Lewis, J. K., I. Shulman, and A. F. Blumberg (1998), Assimilation of Doppler radar current data into numerical ocean models, *Cont. Shelf Res.*, *18*, 541–559.
- Miller, R. N., and M. A. Cane (1989), A Kalman filter analysis of sea level height in the tropical Pacific, *J. Phys. Oceanogr.*, *19*, 773–790.
- Molcard, A., L. I. Piterburg, A. Griffa, T. M. Özgökmen, and A. J. Mariano (2003), Assimilation of drifter observations for the reconstruction of the Eulerian circulation field, *J. Geophys. Res.*, *108*(C3), 3056, doi:10.1029/2001JC001240.
- Moore, A. M., H. G. Arango, E. Di Lorenzo, B. D. Cornuelle, A. J. Miller, and D. J. Neilson (2004), A comprehensive ocean prediction and analysis system based on the tangent linear and adjoint of a regional ocean model, *Ocean Modell.*, *7*, 227–258.
- Oke, P. R., J. S. Allen, R. N. Miller, G. D. Egbert, and P. M. Kosro (2002a), Assimilation of surface velocity data into a primitive equation coastal ocean model, *J. Geophys. Res.*, *107*(C9), 3122, doi:10.1029/2000JC000511.
- Oke, P. R., J. S. Allen, R. N. Miller, G. D. Egbert, J. A. Austin, J. A. Barth, T. J. Boyd, P. M. Kosro, and M. D. Levine (2002b), A modeling study of the three-dimensional continental shelf circulation off Oregon, I, Model-data comparisons, *J. Phys. Oceanogr.*, *32*, 1360–1382.
- Oke, P. R., J. S. Allen, R. N. Miller, and G. D. Egbert (2002c), A modeling study of the three-dimensional continental shelf circulation off Oregon, II, Dynamical balances, *J. Phys. Oceanogr.*, *32*, 1383–1403.
- Oliger, J., and A. Sundström (1978), Theoretical and practical aspects of some initial boundary value problems in fluid dynamics, *SIAM J. Appl. Math.*, *35*, 419–446.
- Pierce, S. D., R. L. Smith, P. M. Kosro, J. A. Barth, and C. D. Wilson (2000), Continuity of the poleward undercurrent along the eastern boundary of the mid-latitude North Pacific, *Deep Sea Res.*, *47*, 811–829.
- Scott, R. K., J. S. Allen, G. D. Egbert, and R. N. Miller (2000), Assimilation of surface current measurements in a coastal ocean model, *J. Phys. Oceanogr.*, *30*, 2359–2378.
- Yaremchuk, M. I., and N. A. Maximenko (2002), A dynamically consistent analysis of the mesoscale eddy field at the western North Pacific Subarctic Front, *J. Geophys. Res.*, *107*(C12), 3223, doi:10.1029/2002JC001379.

---

J. S. Allen, T. Boyd, G. D. Egbert, P. M. Kosro, A. L. Kurapov, R. M. Levine, and N. Miller, College of Oceanic and Atmospheric Sciences, Oregon State University, 104 Ocean Administrative Building, Corvallis, OR 97331, USA. (jallen@coas.oregonstate.edu; tboyd@coas.oregonstate.edu; egbert@coas.oregonstate.edu; kosro@coas.oregonstate.edu; kurapov@coas.oregonstate.edu; mlevine@coas.oregonstate.edu; miller@coas.oregonstate.edu)